

Analysis and experimental investigation of Apollo sample 12032,366-18, a chemically evolved basalt from the Moon

Amanda C. STADERMANN ^{*}1, Bradley L. JOLLIFF², Michael J. KRAWCZYNSKI²,
 Christopher W. HAMILTON ¹, and Jessica J. BARNES¹

¹Lunar and Planetary Laboratory, University of Arizona, 1629 E. University Blvd, Tucson, Arizona 85721, USA

²Department of Earth and Planetary Sciences & McDonnell Center for Space Sciences, Washington University in St. Louis, 1 Brookings Dr, St. Louis, Missouri 63130, USA

*Corresponding author. E-mail: stadermann@email.arizona.edu

(Received 09 April 2021; revision accepted 07 February 2022)

Abstract—Sample 12032,366-18 is a 41.2 mg basaltic rock fragment collected during the Apollo 12 mission to the Moon. It is enriched in incompatible trace elements (e.g., 7 ppm Th), but does not have a bulk composition that would be considered a KREEP (enriched in potassium, rare earth elements, and phosphorous) basalt. The sample is of particular interest because it may be representative of some of the mare basalts within Oceanus Procellarum that are inferred to be Th-rich, based on remote sensing data. The major mineral assemblage of 12032,366-18 is pyroxene, plagioclase, olivine, and ilmenite, and the bulk composition has 4.2 wt% TiO₂, 11.7 wt% Al₂O₃, and 0.25 wt% K₂O. The sample contains regions of late-stage crystallized minerals and glass (collectively termed mesostasis), including K-feldspar, apatite, rare earth (RE) merrillite, ilmenite, troilite, silica, and relatively sodic plagioclase adjacent to ferroan pyroxene. The mesostasis also occurs in several areas that are highly enriched in silica and intergrown with K-feldspar and very fine-grained, high-mean-atomic-number phases. We explore the petrology of this sample, including the origin of the Si-K-rich mesostasis to assess whether the mesostasis had formed by silicate liquid immiscibility (SLI). We used experiments to determine if the bulk composition of 12032,366-18 is representative of a bulk liquid composition, how the residual liquid evolves, and to investigate the partitioning of elements between phases as the melt evolves. Experiments support that the mesostasis formed by SLI after crystallization of minerals closely matches the major-mineral assemblage of 12032,366-18. Experiments bracket the onset of SLI and merrillite saturation between 1024 and 1002 °C. Some high field strength elements, such as Zr and P, partition preferentially into the Fe-rich liquid. From the experiments, we infer that the bulk composition of 12032,366-18 represents the magma from which it crystallized. Based on the Th-rich and KREEP-bearing chemistry of this sample, along with experimental evidence showing that the sample is representative of a bulk liquid composition and not a cumulate, we conclude that basalt fragment 12032,366-18 was delivered to the Apollo 12 landing site as ejecta from a distant impact and could represent an Oceanus Procellarum basalt. Missions to Oceanus Procellarum, such as Chang'E 5, have the potential to confirm whether some of those basalts are indeed enriched in Th and other incompatible trace elements as indicated by remote sensing.

INTRODUCTION

Mare basalts account for more than a fifth of the lunar samples returned from the Apollo missions. The

Apollo 12 samples include three main suites of basalts: olivine basalts, ilmenite basalts, and pigeonite basalts (Hallis et al., 2014; Neal & Taylor, 1992; Rhodes et al., 1977). All of the suites are considered low-Ti, with TiO₂

generally <5 wt%, and low in K (<1000 ppm) and <11 wt% Al₂O₃ (Neal et al., 1994). The Apollo 12 basalt collection also includes a feldspathic basalt, 12038 (Meyer, 2011).

We investigated an Apollo 12 mare basalt rock fragment found in a regolith sample (12032) that is unlike any of these main Apollo 12 basalt types and is likely exotic to the site (Jolliff et al., 2005). It has a trace-element-rich composition, but is not a KREEP basalt, as explained in the Results and Discussion sections. It has 19.5 wt% FeO and 11.7 wt% Al₂O₃, making it more like mare basalts than the known KREEP basalts. For these reasons, we describe the sample as KREEP-bearing to indicate it is trace-element-rich but has a bulk composition different than Apollo 15 and 17 KREEP basalts. The lithology includes felsic (Si+K-rich) regions that may be indicative of a process such as silicate liquid immiscibility (SLI), metasomatic enrichment, or assimilation (Kramer & Neal, 2003; Neal & Taylor, 1989).

Studying Apollo basalt 12032,366-18 allows us to understand late-stage KREEP-bearing basalts and the impact of SLI on the evolution of lunar magmas (Gullikson et al., 2016; Veksler et al., 2007; Warren & Wasson, 1979). The late-stage or residual melt crystallizes in small, interstitial pockets or mesostasis. These interstitial regions are where accessory phases such as apatite, rare earth (RE) merrillite, zircon, and tranquillityite typically occur (Tartèse, Anand, & Delhaye, 2013; Yoder, 1979). These phases are important for understanding the volatile content of the Moon (apatite; e.g., McCubbin et al., 2015; Tartèse, Anand, Barnes, et al., 2013) as well as for geochronology (apatite, RE-merrillite, baddelyeite, and tranquillityite; e.g., Snape et al., 2016; Tartèse, Anand, & Delhaye, 2013). We seek to better understand the magmatic history of a compositionally evolved lunar basalt.

The Apollo 12 mission landed on November 24, 1969, in southeastern Oceanus Procellarum, at a landing site within a prominent secondary ray from Copernicus, but also within reach of ray material from Kepler crater (Fig. 1a) (Korotev et al., 2011). Western and northern Oceanus Procellarum are known for their geologically young basalt flows, as young as 1.0 Ga according to crater size frequency distribution analysis (Hiesinger et al., 2003; Qian et al., 2018; Stadermann et al., 2018). Remotely sensed compositional studies of these late-stage basalt flows suggest that they are relatively rich in thorium (Jolliff et al., 2001; Lawrence et al., 2000), high in iron (Lawrence et al., 2002), and have abundant ilmenite and olivine (Gillis et al., 2003; Pieters et al., 1980; Staid & Pieters, 2001). Basalt fragment 12032,366-18 shares some of these characteristics and thus could

represent one of the evolved mare basalts of Oceanus Procellarum.

We address the following three questions. (1) Is the bulk composition of the sample 12032,366-18 representative of the liquid from which it crystallized? (2) How did the residual melt evolve as this basalt crystallized and what bearing does the incompatible-element enrichment of the basalt have on the residual melt crystallization? (3) If immiscible residual liquids were involved, how do minor and trace elements partition between these liquids, a process which may affect late-stage mineral chemistry? Addressing these questions contributes to a better understanding of the processes by which low-Ti lunar magmas crystallized, in addition to better understanding the origin of this basalt fragment.

SAMPLE DESCRIPTION

Apollo 12 regolith soil sample 12032 was collected on the Moon from the north rim of Bench Crater. This 310.5 g sample has an average grain size of 108 μm and a maturity index ($I_S/FeO = 12$) indicating an immature to very-immature soil (McKay et al., 1971). The 12032 soil sample is poorly sorted, with fragments up to 4 mm. In the 0.6–1 mm size fraction, a large portion (25–50%) of the grains consist of “ropy glass” (Marvin et al., 1971). The ropy glass was studied in detail by Wentworth et al. (1994), who determined ⁴⁰Ar-³⁹Ar degassing ages of $\sim 800 \pm 15$ Ma, and inferred that these glasses originated from the Copernicus impact event.

The focus of this study is a particular basaltic rock fragment analyzed as part of a split of 2–4 mm rock fragments numbered 12032,366 (Korotev et al., 2011). The rock fragment was designated 12032,366-18 and was initially described by Jolliff et al. (2005). Following instrumental neutron activation analysis (INAA), 12032,366-18 was sawn in two (Fig. 1b). A portion of the sample was made into a polished mount, and analyzed by Jolliff et al. (2005), and a subsample was analyzed by Barra et al. (2006) for ⁴⁰Ar-³⁹Ar age determination. They analyzed two splits (A, 1.884 mg and B, 0.338 mg). Split A yielded degassing ages of 548 ± 21 Ma, 688 ± 10 Ma, and 2329 ± 48 Ma, while split B yielded degassing ages of 487 ± 41 Ma and 2736 ± 210 Ma. The ~ 2.3 Ga age was interpreted as a minimum crystallization age, whereas the younger ages, ~ 500 – 700 Ma, could be disturbance ages that may be distinct from the ~ 700 – 800 Ma event that characterizes many other samples from the Apollo 12 landing site. Our work presents results that include those presented in Jolliff et al. (2005) and additional detailed petrologic study of basalt fragment 12032,366-18.

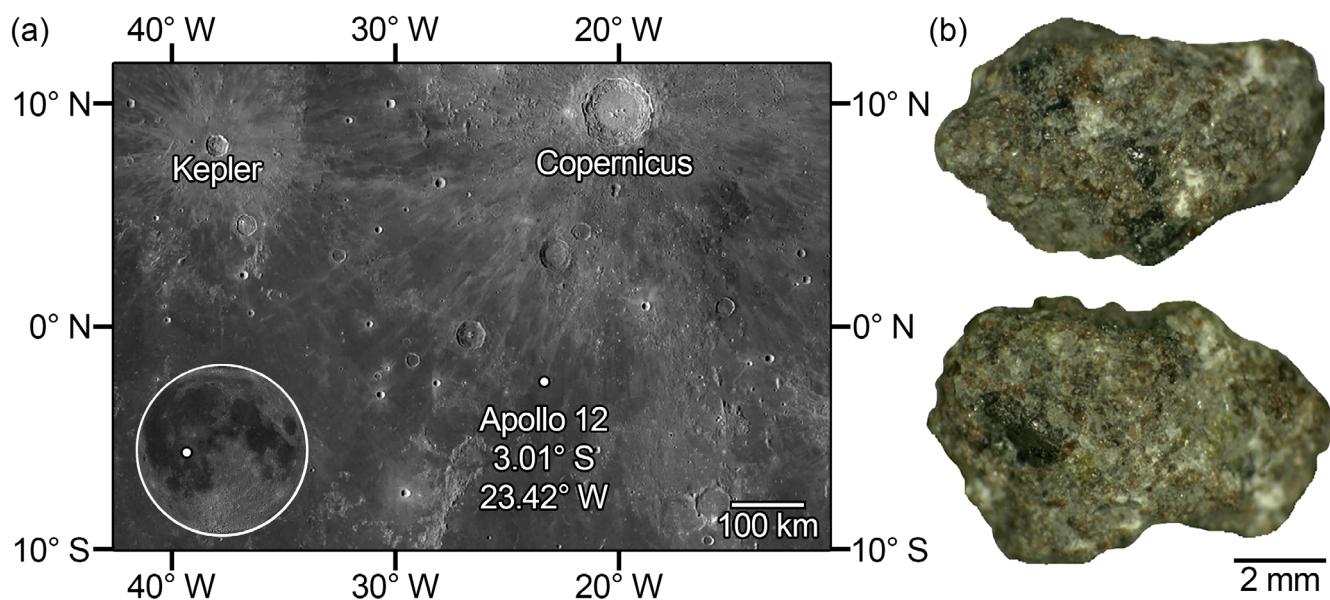


Fig. 1. a) Lunar Reconnaissance Orbiter Camera (LROC) Wide Angle Camera (WAC) Global Morphologic basemap mosaic of the region surrounding the Apollo 12 landing site. Apollo 12 location, noted by the white dot, is in a secondary ray from Copernicus crater. Both context and local images acquired via the Lunar QuickMap: quickmap.lroc.asu.edu. Basemap credit to NASA/GSFC/Arizona State University. b) Optical image of sawn halves of 12032,366-18 following instrumental neutron activation analysis (INAA) and cool down. (Color figure can be viewed at wileyonlinelibrary.com.)

METHODS

Sample 12032,366-18 was first irradiated for analysis of bulk major- and trace-element concentrations via INAA, as described in the Instrumental Neutron Activation Analysis section. The sample was then sawn in two at Washington University in St. Louis using a slow-speed diamond wafer saw with de-ionized water as a lubricant. One portion was analyzed at the University of Arizona for ^{40}Ar - ^{39}Ar age determination (Barra et al., 2006). The other portion was mounted in epoxy and polished at Washington University in St. Louis. We analyzed the polished grain mount of 12032,366-18 using electron probe microanalysis (EPMA), with techniques and standards described in the Electron Probe Microanalysis section. Then, modal recombination was used to obtain the bulk composition. Using the experimental methods described in the following section, we performed experiments to mimic the fractional crystallization sequence of a liquid similar to 12032,366-18. Experimental samples were analyzed using EPMA, as described in the Electron Probe Microanalysis section. Finally, the phase proportions for experiments were modeled using the bulk composition of the experiment and phase compositions.

Instrumental Neutron Activation Analysis

The sample was irradiated for 24 h using the University of Missouri Research Reactor. Using INAA,

the concentrations of 24 major, minor, and trace elements of sample 12032,366-18 were determined. Detailed procedures for INAA and specifically for this sample, the inclusion of flux monitors, were described by Barra et al. (2006), Korotev (1991), and primarily by Korotev et al. (2011).

Electron Probe Microanalysis

Microscopic textures and chemical composition of minerals within both 12032,366-18 and the experimental charges were determined using EPMA. We report compositions determined initially using a JEOL 733 Superprobe with Advanced MicroBeam Inc. automation and later, the JEOL JXA-8200 at Washington University in St. Louis, and the Cameca SX-100 at the Lunar and Planetary Laboratory at the University of Arizona. We obtained back-scattered electron (BSE) images and elemental X-ray maps of the full section and performed spot analyses via EPMA. Standards for each analysis varied depending on the element of interest, the phase under investigation, and the electron probe used when the analysis occurred (i.e., standards used were tailored to maximize the accuracy of each analysis; see supporting information). Primary standards for EPMA included: Gates wollastonite (Si, Ca), San Carlos olivine (Si, Mg), Rockport fayalite (Si, Fe), synthetic TiO_2 (Ti), natural rutile (Ti), Alaska anorthite (Al), Hakone anorthite (Al, Ca), Cr_2O_3 P-585 (Cr),

Smithsonian chromite (Cr), Elba hematite (Fe), synthetic Mn olivine (Mn), rhodonite 104791 (Mn), Shankland forsterite (Mg), Taylor barite (Ba), National Institute of Standards and Technology (NIST) Glass K-458 (Ba), Amelia albite (Na), Crete albite (Na), Madagascar orthoclase (K), Penn State orthoclase OR-1 (K), Durango apatite (P, F), Synthetic fluorapatite (P), Taylor ZrO₂ (Zr), Smithsonian zircon (Zr), Corning glass 95IRV (Ce), yttrium aluminum garnet (Y), Tugtupite (Cl). All analyses were performed using a probe current of 10–30 nA, an accelerating voltage of 15 kV, and beam diameters ranging from 1 to 20 μm , depending on the target mineral or phase. No time-dependent intensity corrections were applied.

Modal Recombination

The modal abundances of phases were determined using BSE images and X-ray maps of the sample in Adobe Photoshop using the histogram tool, which shows the distribution of pixel brightness and can be binned. Intervals of brightness in the images were assigned to mineral phases based on petrologic and geochemical mapping of the sample. Binning the pixel brightness to values corresponding to different minerals, and evaluating the number of pixels in that bin, corresponds to the areal abundance of that mineral in the section. For example, ilmenite has a high mean atomic number and therefore appears bright in the BSE images. Collecting all the pixels with the brightness corresponding to ilmenite, relative to all the pixels in the image, gives the areal ilmenite abundance. The BSE images, with different levels of brightness and contrast, allowed us to check for consistency in this method (minerals receiving the same areal abundance between images), while X-ray maps were used to discriminate different minerals with similar mean atomic numbers.

The mean composition of each phase was then used, in conjunction with the abundance of the phases, to compute the composition of the bulk sample 12032,366-18. For example, ilmenite accounts for 6% of the areal abundance in the section; therefore, 0.06 times the composition of ilmenite gives the component of the bulk composition that derives from ilmenite. Adding this component to the other phases' components gives a total bulk composition that reflects the imaged section and the average compositions of phases in that section.

Several sources for potential uncertainty exist with this method of determining bulk composition. First, we calculated the composition of a three-dimensional rock fragment based on a single two-dimensional slice. Second, using BSE and X-ray images of the section provided us with areal percentages of phases, which were converted to weight percent of oxides using the

average phase composition and density. The use of image analysis relies in part on pixel resolution; in some cases, the pixel size exceeds the size of some crystals, and those pixels along phase boundaries average the phase intensities. These resolution-based issues introduce error into the calculation, estimated to be about 5% of the phase abundance (Maloy & Treiman, 2007). Finally, when minerals exhibit compositional zoning, the average value of the mineral's composition was used to represent the entire phase. This introduces error when the average of analyses was not representative of the volume-based average composition of that phase. However, we found good agreement between the modal recombination data and the INAA values for the elements analyzed by both methods. Performing experiments using the reconstructed bulk composition as a starting material and successfully reproducing the mineral assemblage and composition of minerals in 12032,366-18 is a way to confirm that the bulk composition is representative of the lava flow it originated from and to learn about the temperature interval for crystallization.

Experimental Methods

The bulk composition of the sample 12032,366-18 (see the Modal Recombination section) was taken as the starting composition for our melting and crystallization experiments. To re-create the starting composition of the 12032,366-18 (Table 1), we created a mixture of powdered oxides and other compounds (Tables 2 and S1 in supporting information). We used SiO₂, TiO₂, Al₂O₃, Cr₂O₃, Fe metal sponge, FeO, Fe₂O₃, MnO, Mg(OH)₂, CaCO₃, BaCO₃, Na₂CO₃, K₂CO₃, P₂O₅, AlPO₄, ZrO₂, and ZrSiO₄ to create the starting compositions. We combined these powders thoroughly using a silicon-nitride ball mill with isopropanol and created ~60 mg pellets using polyvinyl alcohol as a binding agent and a hydraulic press. The pellets were then placed on a Re wire loop and hung on a Pt wire thread at the hot spot of a Deltech vertical gas-mixing furnace. Samples were held in a mixture of H₂ and CO₂ for the duration of the experimental run, within ± 0.5 log units of the iron-wüstite (IW) oxygen fugacity (f_{O_2}) buffer, as monitored by a Ca-doped zirconia oxygen probe (Table 3). Our experiments, performed at approximately IW f_{O_2} conditions, were within the range of the availability of oxygen in lunar magmatic systems (IW–2 to IW+1; Sato et al., 1973; Wadhwa, 2008). The H₂:CO₂ ratio for each experiment varied because of the changing temperature of the experiments (Tables 3, S2 in supporting information). The temperatures and duration of experiments ranged between 1106–975 °C and 22–192 h (Table 3). At the end of each run, an electrical

Table 1. 12032,366-18 bulk composition, normalized to 100%.

Oxide	wt%
SiO ₂	44.17
TiO ₂	4.21
Al ₂ O ₃	11.67
Cr ₂ O ₃	0.22
FeO	19.44
MnO	0.26
MgO	7.18
CaO	11.47
BaO	0.06
Na ₂ O	0.69
K ₂ O	0.25
P ₂ O ₅	0.28
ZrO ₂	0.08

Gives molar $Mg/(Mg+Fe) = 0.397$.

current was passed through the Pt thread, melting the Pt thread, and dropping the sample into a beaker of deionized water. Each experiment was broken using pliers and ~6 visually representative pieces were mounted in epoxy resin. Note that any spatial orientation of the sample was lost in this process. After mounting the sample in epoxy, each sample was hand-polished using a diamond suspension solution or SiC grinding paper. Then each sample was coated with an ~22 nm thick layer of carbon for EPMA.

The bulk composition of the second experiment (J024) was based on the average composition of glass in the initial experiment, H028 (Table 2). Similarly, the bulk composition of the remaining experiments (J157, H168, J146) was based on the average glass composition of the J024 experiment. This changing starting composition for the experiments allowed us to produce measurable amounts of glass in lower temperature experiments (Table 3).

The bulk composition of the J157, H168, and J146 experiments included calculated concentrations for BaO, P₂O₅, and ZrO₂. Barium and zirconium were not added to the bulk compositions of the H028 or J024 experiments because their low initial concentration in the sample could not be reliably reproduced in the starting material. Phosphorous was suspected to have been lost in the higher temperature experiments, as evidenced by decreasing concentration of P₂O₅ in the glass despite the lack of phosphorus-bearing phases in those experiments. We used the concentration of K₂O in the glass and other phases in J024 to estimate the partition coefficient of K in olivine, plagioclase, pyroxene, and ilmenite. Combining these partition coefficients with the calculated mode of that phase in the experiment (see the Phase Proportions of Experiments section), we calculated a bulk partition coefficient of K in J024. From this bulk

partition coefficient and an estimate of the system's percent crystallized, we calculated the concentration of Ba, P, and Zr that should have been in the glass at that stage. This calculation is valid with the assumption that Ba, P, and Zr have similar partitioning behavior as K in the early stages of crystallization.

For the three lowest temperature experiments, the bulk composition remained constant, and temperature varied, allowing us to observe the changing mineral chemistry with temperature. The temperature was lowered until the experiments produced a glass composition similar to or approaching the average composition of mesostasis in Apollo sample 12032,366-18 (i.e., ~975 °C in J146).

Phase Proportions of Experiments

Using the mineral and glass compositions obtained via EPMA, we used an isometric log-ratio transform least squares regression algorithm to determine the phase proportions of our experiments. We used a program, Log-ratio Inversion of Mixed Endmembers (LIME), developed by Krawczynski and Olive (2011), to predict the proportions of each phase (including glass) in each experiment. The LIME program was also used to calculate the overall percentage of melt crystallized as we progressed from the first experiment to the last and to understand the appearances and disappearances of minerals in the system. The LIME program benefits from using a log-ratio inversion, which excludes the possibility of negative composition space existing as well as allowing for all the variables in the linear regression to be independent and not constrained by a 100% mass sum. The LIME program has been used in other publications for similar purposes (Gavrilenko et al., 2019; Grove et al., 2013; Prissel et al., 2018).

To understand the evolution of the system as a whole, we estimated the system's total crystallization percentage after each experiment. For H028, this was simply the sum of the crystalline phase proportions from LIME. For J024, the system's total crystallization percentage was calculated by combining the percent crystalline from H028 and the percentage of crystals in J024. Similar calculations were performed for the remaining experiments.

RESULTS

Characterization of 12032,366-18

The ~4-mm-wide, 41.2 mg basalt fragment investigated in this study, 12032,366-18 (Fig. 2), was initially analyzed for major and trace elements by INAA (Table 4) and EPMA (Table 5). The bulk

Table 2. Starting compositions (in wt%) for experiments, normalized to 100%.

Experiment	Source for composition	SiO ₂	TiO ₂	Al ₂ O ₃	Cr ₂ O ₃	FeO	MnO	MgO	CaO	BaO	Na ₂ O	K ₂ O	P ₂ O ₅	ZrO ₂
H028	12032,366-18	44.25	4.22	11.69	0.22	19.48	0.26	7.19	11.49	n.i.	0.69	0.25	0.28	n.i.
J024	H028 glass	45.31	5.59	10.21	0.09	21.14	0.24	4.79	11.07	n.i.	0.79	0.36	0.41	n.i.
J157	J024 glass	50.33	3.55	9.56	0.02	22.03	0.26	1.64	8.94	0.24	1.04	0.92	1.13	0.34
H168	J024 glass	50.33	3.55	9.56	0.02	22.03	0.26	1.64	8.94	0.24	1.04	0.92	1.13	0.34
J146	J024 glass	50.33	3.55	9.56	0.02	22.03	0.26	1.64	8.94	0.24	1.04	0.92	1.13	0.34

n.i. = not included in composition.

Table 3. Run conditions and products for experiments.

Experiment	Duration (h)	log(<i>f</i> /O ₂) (ΔIW)	Resulting phases (calculated mode)	Cumulative crystallization (%)	Comments
H028	22	0 to 0.04	olv (9.4) + plag (12.9) + pyx (10.4) + sp (tr) + liq (67.3)	32.7	Constant temperature throughout entire experiment, 1106 °C.
J024	96	-0.12 to 0.14	olv (10.8) + plag (27.1) + pyx (35.6) + ilm (7.9) + liq (18.5)	87.6	Conditioned mix: pre-cooked to get rid of starting material and homogenize the mixture. Constant temperature throughout entire experiment, 1050 °C.
J157	168	-0.27 to -0.25	plag (1.5) + pyx (1.7) + ilm (0.5) + sil (1.5) + liq (94.8)	88.2	Took to 1075 °C for 12 h, then cooled at -1 °C h ⁻¹ to final temperature, 1024 °C, then held for remaining time.
H168	192	-0.36 to -0.23	olv (13.7) + plag (21.9) + pyx (14.8) + ilm (5.3) + sil (9.1) + merr (1.6) + Lfe (12.4) + Lsi (21.2)	95.8	Took to 1075 °C for 12 h, then cooled at -1 °C h ⁻¹ to final temperature, 1002 °C, then held for remaining time.
J146	163	-0.41 to -0.36	olv (9.7) + plag (23.8) + pyx (30.0) + ilm (5.3) + sil (10.5) + merr (1.9) + bdy (tr) + Lfe (7.3) + Lsi (11.5)	97.7	Took to 1075 °C for 12 h, then cooled at -1 °C h ⁻¹ to final temperature, 975 °C, then held for remaining time.

olv = olivine; plag = plagioclase; pyx = pyroxene; sp = spinel; liq = residual liquid; ilm = ilmenite; sil = silica; merr = merrillite; Lfe = iron-enriched liquid; Lsi = silica-enriched liquid; bdy = baddeleyite; tr = trace, not included in LIME calculations.

composition of 12032,366-18 has a high concentration of FeO (19.5 wt%), well in the range for mare basalts (~16–23 wt%) and higher than Apollo 15 and Apollo 17 KREEP basalts (~9–15 wt%; Fig. 3). Its Al₂O₃ content (11.7 wt%) is lower than in KREEP basalts (13–15 wt%) and the TiO₂ content (4.2 wt%) is higher (compared to 1.0–2.2 wt%), but both Al and Ti are in the range for these elements in known mare basalts (Fig. 3). Consistent with high modal clinopyroxene, the molar Ca/Al, 1.8, is also within the range for mare basalts (1.4–2.4) and is greater than that in KREEP basalts (0.9–1.4). Basalt 12032,366-18 has higher incompatible

trace elements than any of the Apollo or Luna basalts, but on average, only 0.68 times the concentrations in KREEP basalts (Wieczorek et al., 2006).

This sample is an olivine-bearing, clinopyroxene-rich, relatively aluminous basalt with an intermediate Ti content. It contains a 400 μm olivine grain (Fo₁₆) and smaller (<100 μm) occurrences of olivine (Fo_{15–38}) that are, when in contact with pyroxene, in what appears to be a reaction (i.e., resorption) relationship (Fig. 4d). Olivine grains in contact with plagioclase have sharp boundaries (Fig. 4d). Pigeonite and augite are present, ranging in composition from Mg/(Mg+Fe) = 0.68

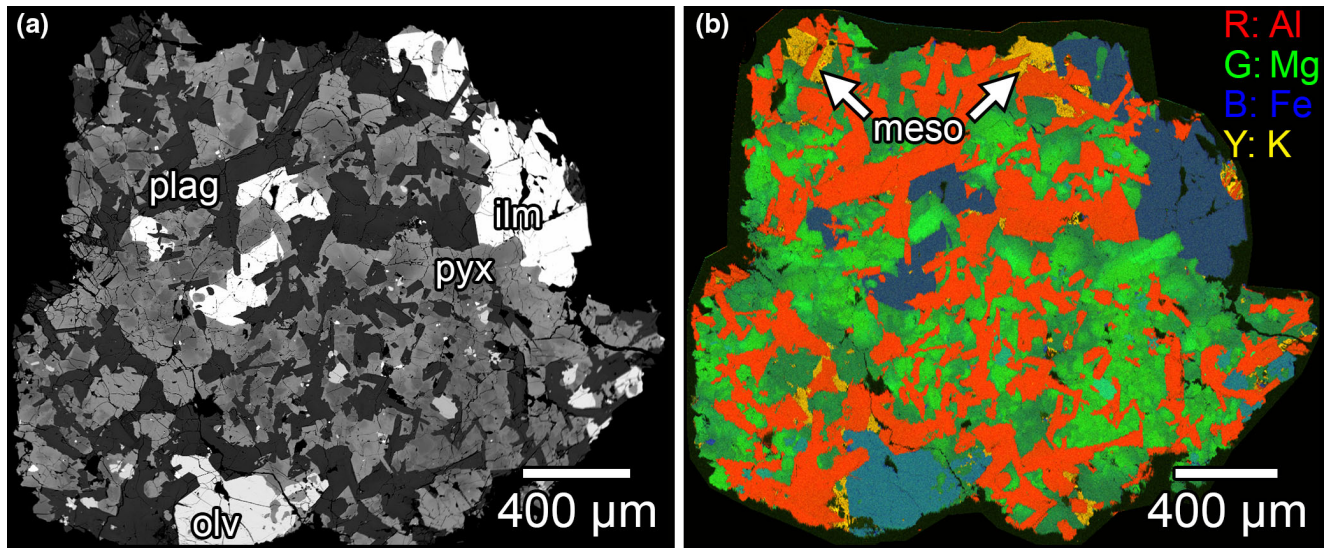


Fig. 2. a) Backscattered electron (BSE) image showing the crystalline, non-vesicular, medium grained, subophitic texture dominated by clinopyroxene (50% by weight) and plagioclase (33%), with relatively coarse ilmenite grains (7%). Olivine makes up 8%, with one large grain (labelled) and small blebs within pyroxene. b) X-ray composite of the sample, with the red representing Al, green representing Mg, blue representing Fe, and yellow representing K. With this scheme, plagioclase appears red; pyroxene, green; olivine, teal; ilmenite, dark blue; and mesostasis, yellow. Two areas of silica-rich mesostasis are noted by arrows. plag = plagioclase; ilm = ilmenite; pyx = pyroxene; olv = olivine; meso = mesostasis. (Color figure can be viewed at wileyonlinelibrary.com.)

Table 4. Bulk abundances of elements and oxides acquired via instrumental neutron activation analysis (INAA).

Element or oxide (units)	Concentration	Uncertainty
Na ₂ O	0.783 wt%	0.008 wt%
CaO	12.7 wt%	0.5 wt%
FeO	19.69 wt%	0.2 wt%
Sc	52.5 μg g ⁻¹	0.5 μg g ⁻¹
Cr	1356 μg g ⁻¹	14 μg g ⁻¹
Co	30.6 μg g ⁻¹	0.3 μg g ⁻¹
Ni	<80 μg g ⁻¹	40 μg g ⁻¹
Rb	<12 μg g ⁻¹	3.4 μg g ⁻¹
Sr	270 μg g ⁻¹	30 μg g ⁻¹
Zr	600 μg g ⁻¹	40 μg g ⁻¹
Cs	0.31 μg g ⁻¹	0.05 μg g ⁻¹
Ba	502 μg g ⁻¹	14 μg g ⁻¹
La	41.2 μg g ⁻¹	0.41 μg g ⁻¹
Ce	105.9 μg g ⁻¹	1.1 μg g ⁻¹
Nd	69 μg g ⁻¹	3.6 μg g ⁻¹
Sm	20.3 μg g ⁻¹	0.2 μg g ⁻¹
Eu	2.9 μg g ⁻¹	0.031 μg g ⁻¹
Tb	4.35 μg g ⁻¹	0.043 μg g ⁻¹
Yb	15.23 μg g ⁻¹	0.15 μg g ⁻¹
Lu	2.11 μg g ⁻¹	0.02 μg g ⁻¹
Hf	15.66 μg g ⁻¹	0.16 μg g ⁻¹
Ta	1.84 μg g ⁻¹	0.066 μg g ⁻¹
Th	6.92 μg g ⁻¹	0.07 μg g ⁻¹
U	1.66 μg g ⁻¹	0.12 μg g ⁻¹

(augite) and 0.58 (pigeonite) to 0.27 in the most ferroan grains (Table 5). In cross section, plagioclase grains range up to ~150 μm in width and 500 μm in length. Plagioclase grains are strongly zoned, with compositions ranging from ~An₉₀ to An₆₀. The most sodic plagioclase (An₅₄Ab₄₃Or₃Cn_{<0.5}) occurs in mesostasis regions. Pyroxene partially encloses plagioclase in a subophitic texture (Fig. 4c). Ilmenite grains are up to ~500 μm in length and compositionally homogenous (Fig. 2).

The minor phases in sample 12032,366-18 include chromian ulvöspinel, titanian chromite, troilite, barian K-feldspar, silica, rare earth merrillite (RE-merrillite), apatite, zircon, and ferro-pyroxene. These phases occur in mesostasis pockets (Figs. 4a, 4b, 4e, and 4f). Apatite in the sample contains 2.66 wt% F and 0.27 wt% Cl corresponding to a missing component of 0.25 atoms per formula unit (apfu; Table 5). We measured Ce and Y in the RE-merrillite and apatite phases. In the merrillite phase, we extrapolated the Ce₂O₃ and Y₂O₃ values, to estimate that the other rare earth element (REE) oxides make up approximately 5.7 wt% of the oxide total. This was done by fitting the other REEs to Ce and Y values in the analyses to create a smooth chondrite-normalized pattern (McCubbin et al., 2011). In addition to the most sodic plagioclase, the felsic mesostasis regions include barian K-feldspar (Cn₇₋₁₄), silica, and very fine grains of what were inferred to be the above minor minerals, some <1 μm. Using a 20 μm

Table 5. Compositions of phases in 12032,366-18, with standard deviations. Full data and uncertainties in Tables S3–S19.

Phase	Number of analyses	Beam diameter (μm)	Mean composition in wt%															Total		
			SiO ₂	TiO ₂	Al ₂ O ₃	Cr ₂ O ₃	FeO	MnO	MgO	CaO	BaO	Na ₂ O	K ₂ O	P ₂ O ₅	ZrO ₂	Y ₂ O ₃	Ce ₂ O ₃		F	Cl
Olv	30	1–10	31.89	0.10	0.01	0.03	57.84	0.56	9.61	0.30	n.a.	0.01	n.a.	0.08	n.a.	n.a.	n.a.	n.a.	n.a.	100.39
			0.88	0.03	0.01	0.02	4.20	0.06	3.35	0.05	0.01	0.01	0.06							0.45
Aug	39	1–5	49.26	1.08	1.48	0.35	22.79	0.34	10.40	13.69	n.a.	0.07	n.d.	n.d.	n.a.	n.a.	n.a.	n.a.	n.a.	99.45
			1.28	0.24	0.66	0.21	6.07	0.09	2.71	2.55	0.02									1.15
Pig	11	1	48.42	0.74	0.84	0.18	30.84	0.45	9.81	7.50	n.a.	0.03	n.a.	n.a.	n.a.	n.a.	n.a.	n.a.	n.a.	98.80
			1.31	0.12	0.15	0.07	3.25	0.04	2.55	1.40	0.02									0.95
Fs	6	1–3	47.62	0.79	0.57	0.07	38.26	0.50	5.98	5.22	0.04	0.01	0.09	0.12	0.17	n.a.	n.a.	n.a.	n.a.	99.28
			0.92	0.14	0.05	0.04	1.63	0.02	0.81	1.13	0.02	0.01	0.05	0.16	0.20					1.27
Plag	121	1–10	47.94	0.07	32.72	0.01	0.74	0.01	0.08	16.02	n.a.	2.20	0.23	n.a.	n.a.	n.a.	n.a.	n.a.	n.a.	99.88
			2.48	0.04	1.72	0.02	0.29	0.01	0.07	1.74	0.81	0.13	0.13							1.01
Ilm	11	3–5	n.d.	52.49	0.06	0.43	45.02	0.35	0.92	0.07	n.a.	n.d.	n.a.	n.a.	n.a.	n.a.	n.a.	n.a.	n.a.	99.36
				0.39	0.02	0.06	0.54	0.04	0.07	0.07										0.82
Ba-K-flt	8	3–5	60.20	0.19	20.55	n.a.	0.48	0.02	0.05	0.92	5.17	2.04	10.61	0.14	n.a.	n.a.	n.a.	n.a.	n.a.	100.24
			1.50	0.12	0.69		0.44	0.03	0.07	0.51	0.92	0.20	1.07	0.16						0.24
K-flt	2	1	64.52	0.10	20.36	n.a.	0.22	n.a.	n.d.	1.82	0.31	2.45	10.23	0.02	0.02	n.a.	n.a.	n.a.	n.a.	99.87
			1.56	0.04	3.31		0.15			2.14	0.84	3.74								0.69
Ti-chr	2	1	0.05	14.45	7.38	27.02	46.03	0.31	1.06	0.43	n.a.	n.d.	n.d.	n.d.	n.a.	n.a.	n.a.	n.a.	n.a.	96.77
			0.00	0.09	0.13	0.04	0.11	0.02	0.01	0.01										0.01
Cr-usp	7	1–5	0.05	26.24	2.55	11.37	55.88	0.34	0.97	0.37	n.a.	n.d.	n.d.	n.d.	n.a.	n.a.	n.a.	n.a.	n.a.	97.79
			0.04	1.14	0.36	2.38	2.07	0.04	0.29	0.06										1.08
Merr	4	1–3	0.65	n.a.	0.13	n.a.	3.59	0.08	1.96	39.59	n.a.	0.19	n.a.	41.77	n.a.	2.37	3.76	0.61	n.d.	94.65
			0.55		0.10		0.06	0.01	0.11	0.55	0.04			0.57		0.35	0.20	0.06		0.85
Apt	3	3	0.62	n.a.	n.d.	n.a.	0.69	0.05	0.03	55.35	n.a.	0.07	n.a.	40.92	n.a.	0.37	0.63	2.66	0.27	101.66
			0.21				0.10	0.02	0.00	0.22	0.01			0.28		0.05	0.11	0.12	0.02	0.24
Sil	2	1–3	100.71	0.23	0.52	n.d.	0.39	n.d.	n.d.	0.10	n.a.	0.09	n.d.	n.d.	n.d.	n.a.	n.a.	n.a.	n.a.	102.08
			0.02	0.02	0.07		0.21			0.03	0.01									0.33
Felsic meso	25	1–20	78.31	0.38	11.42	n.d.	0.71	0.03	0.05	0.71	n.a.	1.27	6.50	0.09	0.11	n.a.	n.a.	n.a.	n.a.	99.45
			1.99	0.14	1.32		0.48	0.01	0.08	0.64	0.19		1.45	0.05	0.07					0.79
Mafic meso	2	3	33.49	0.81	0.82	0.13	24.80	0.34	5.89	17.19	0.14	0.15	0.23	15.31	n.a.	n.a.	n.a.	n.a.	n.a.	99.23
			7.41	0.22	0.36	0.00	5.45	0.09	0.17	5.86	0.03		0.28	7.17						1.07

olv = olivine; aug = augite; pig = pigeonite; fs = ferrosilite; plag = plagioclase; ilm = ilmenite; fld = feldspar; chr = chromite; usp = ulvöspinel; merr = merrillite; apt = apatite; sil = silica; meso = mesostasis; n.d. = not detected; n.a. = not analyzed.

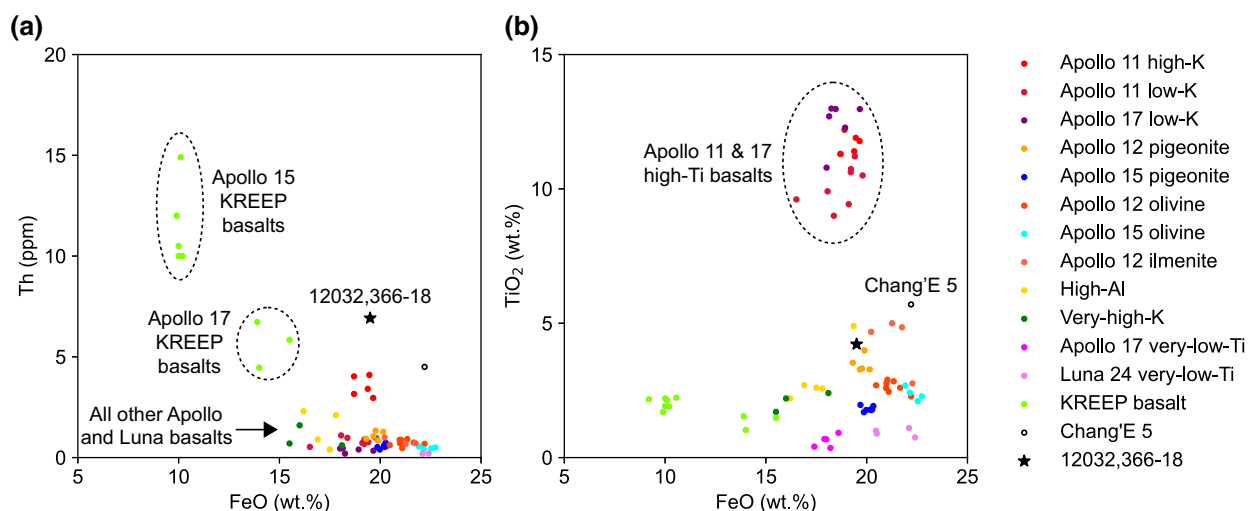


Fig. 3. a) Bulk thorium abundance versus bulk FeO content in Apollo, Luna, and Chang'E 5 mare and KREEP basalts including 12032,366-18, indicated by a black star. b) Bulk TiO_2 content versus bulk FeO content in Apollo and Luna mare and KREEP basalts. Sample 12032,366-18 is insufficiently depleted in FeO to be considered a KREEP basalt, and plots well within the mare basalt field in (b). Apollo and Luna data from Wiczorek et al. (2006); Chang'E 5 data from Tian et al. (2021). (Color figure can be viewed at wileyonlinelibrary.com.)

diameter electron beam, we found that the bulk composition of these mesostasis areas reach 76–79 wt% SiO_2 , with the remainder predominantly Al_2O_3 (~11 wt%), K_2O (6–7 wt%), and Na_2O (1.5 wt%). In addition to felsic mesostasis, there are limited occurrences of mafic mesostasis, of which we obtained two analyses (Figs. 4b and 4f). These two analyses vary significantly from each other, with compositions of 28 wt% SiO_2 , 21 wt% FeO, 21 wt% CaO, and 20 wt% P_2O_5 and 39 wt% SiO_2 , 29 wt% FeO, 13 wt% CaO, and 10 wt% P_2O_5 , respectively. These two mafic mesostasis analyses are located adjacent to two occurrences of felsic mesostasis.

Experimental Results

The phases found in each experiment, their calculated mode (Fig. 5), the average compositions of those phases presented in Table 6, and the system's percentage of crystallization after each experiment are presented in Table 3. Figure 6 shows representative BSE images of each experiment.

In H028, we observed olivine, plagioclase, pyroxene, and chromian ulvöspinel, along with quenched glass (Table 6). Olivine has an intermediate composition (Fa_{45-46}). Plagioclase is calcic and only slightly zoned (An_{81-85} , $\text{Or}_{<1}$). The pyroxenes are slightly magnesian and augitic ($\text{En}_{42}\text{Wo}_{37}\text{Fs}_{21}$ to $\text{En}_{42}\text{Wo}_{33}\text{Fs}_{25}$) and contain up to 3 wt% TiO_2 . The glass has 44–45 wt% SiO_2 . Using LIME, we found that approximately 67.3 wt% of the sample is glass, indicating that the overall percentage crystallized was 32.7 wt% (Table 3).

In J024, we started with the glass composition of H028. The phases olivine, plagioclase, pyroxene, ilmenite, and quenched glass are identified in J024. Olivine is significantly more Fe-rich than the previous experiment at Fa_{73-76} . Experiment J024 presents zoned pyroxenes and plagioclases. The plagioclase ranges in composition from An_{64} to An_{76} , with $\text{Or}_{<2}$. The pyroxene crystals are also zoned, with compositions ranging $\text{En}_{32}\text{Wo}_{39}\text{Fs}_{29}$ to $\text{En}_{32}\text{Wo}_{17}\text{Fs}_{51}$ (Fig. 7). The glass in J024 contains ~5 wt% more SiO_2 than in H028. Other oxides that increased in the glass include FeO, Na_2O , K_2O , while TiO_2 , Al_2O_3 , Cr_2O_3 , and MgO decreased (Fig. 8). Using LIME, we found that 18.5 wt% of the sample is glass, indicating that 87.6 wt% of the overall system (combining H028 and J024) had crystallized (Table 3).

The average glass composition of J024 provided the starting composition for the remaining experiments. This starting composition allowed us to assess how the glass composition (i.e., that of the residual liquid) evolved in detail across the entire cooling interval.

In J157, we observed plagioclase, pyroxene, ilmenite, silica, and glass (Fig. 6c). A single plagioclase crystal was observed, approximately 200 μm in length, with a nearly uniform composition of An_{60-62} , with approximately $\text{Or}_{1.4}$. Pyroxene crystals were small and therefore not significantly zoned. However, intracrystal variation led to compositions ranging from $\text{En}_{29}\text{Fs}_{56}\text{Wo}_{15}$ to $\text{En}_{23}\text{Fs}_{36}\text{Wo}_{41}$. Glass composition was fairly consistent and very similar to the average glass composition from J024. This is consistent with the finding that the experiment was 94.8% glass. The LIME

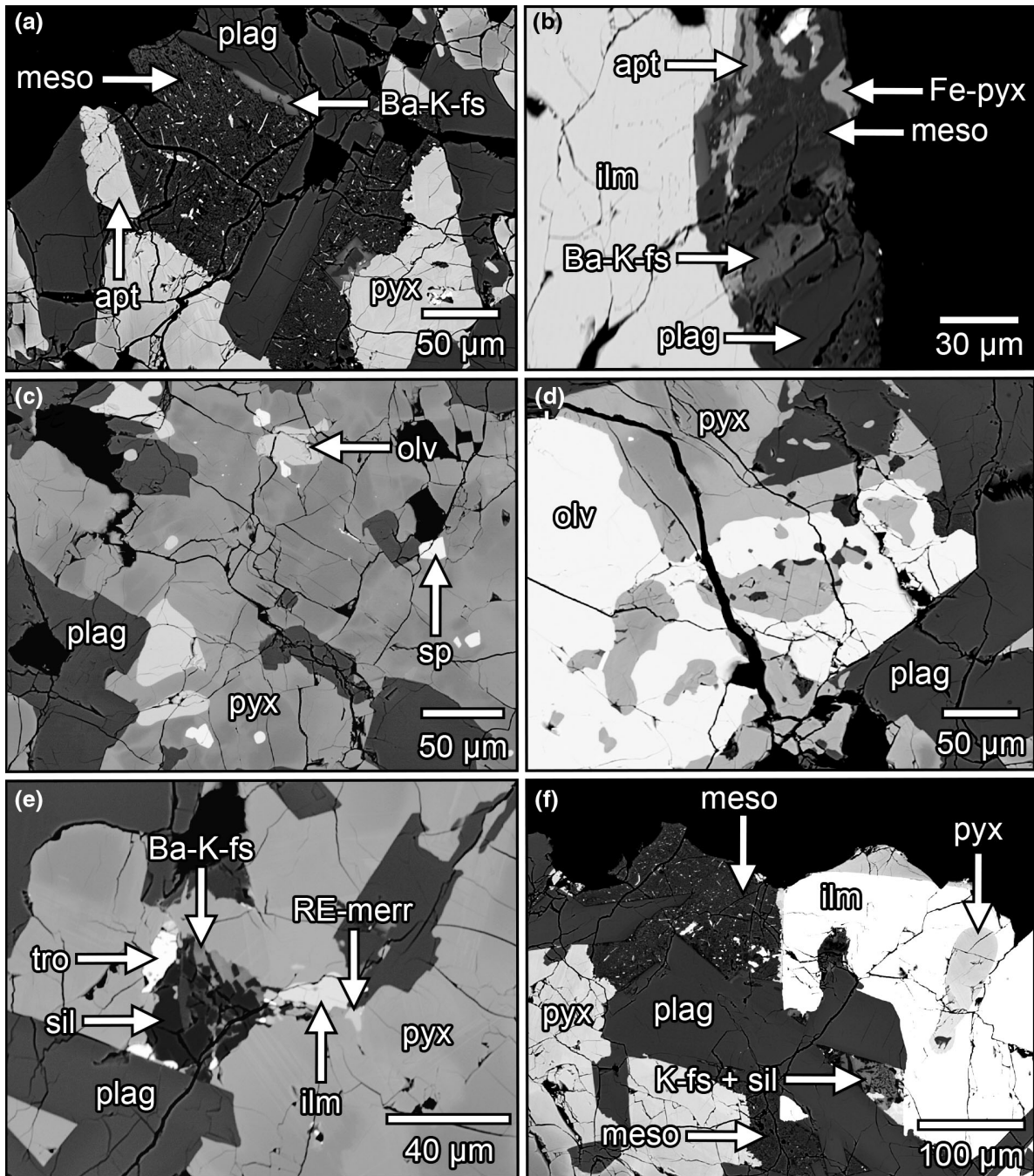


Fig. 4. BSE images of sample 12032,366-18. a) Si+K-rich mesostasis with intergrown Si-rich and K-rich phases plus high-Z (atomic number) phases including ilmenite, a Zr-rich phase, apatite, and ferro-pyroxene, plus several discrete grains of Ba-K-feldspar. b) Mesostasis region with Ba-K-feldspar, ferro-pyroxene, apatite, and Na-rich plagioclase. Mafic mesostasis also occurs in this region. c) Pyroxene enclosing plagioclase, along with olivine and ulvöspinel. d) Olivine in a reaction (i.e., resorption) relationship with pyroxene, with olivine showing irregular boundaries with pyroxene but sharp boundaries with plagioclase. e) Small pocket of crystallized residual melt comprising ilmenite, silica, Ba-K-feldspar, troilite, plagioclase, and phosphates (RE-merrillite and apatite). f) Two mesostasis regions similar to (a), one with a region of intergrown silica and K-feldspar. Lower mesostasis region contains occurrence of mafic mesostasis. Note the change in scale bar between panels. Plag = plagioclase; Ba-K-fs = barian K-feldspar; meso = mesostasis; apt = apatite; pyx = pyroxene; Fe-pyx = ferro-pyroxene; ilm = ilmenite; olv = olivine; sp = ulvöspinel; RE-merr = RE-merrillite; tro = troilite; sil = silica; K-fs = potassium feldspar.

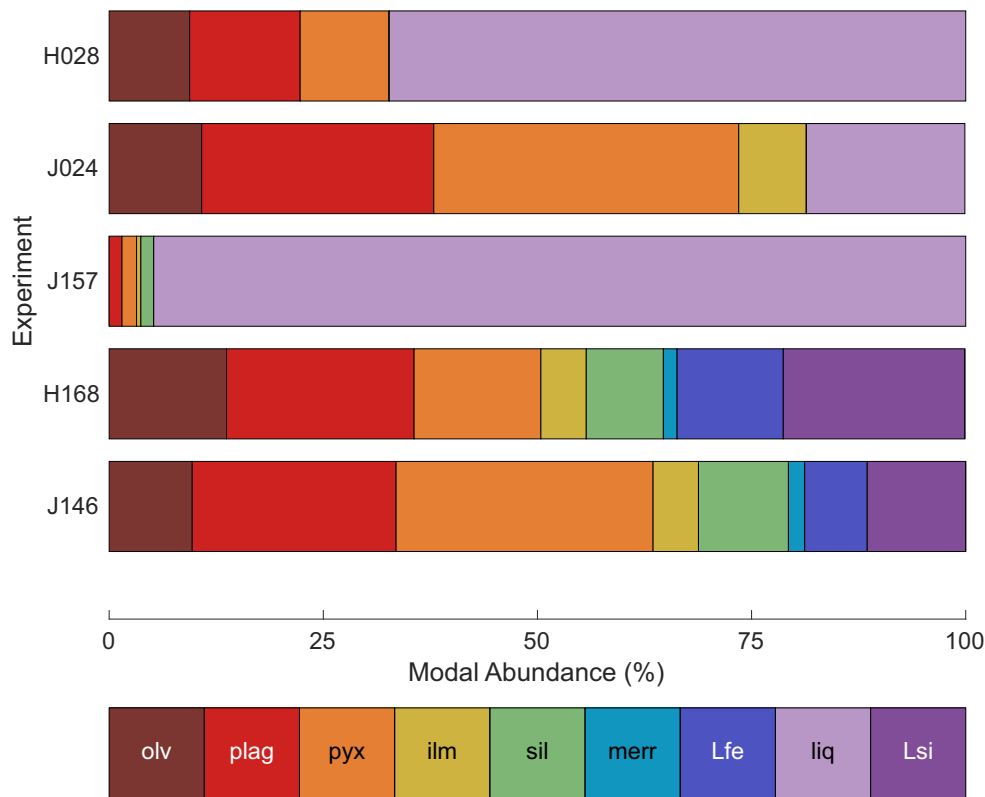


Fig. 5. Abundance of phases in experiments. olv = olivine; plag = plagioclase; pyx = pyroxene; ilm = ilmenite; sil = silica; merr = merrillite; Lfe = iron-enriched liquid; liq = liquid; Lsi = silica-enriched liquid. (Color figure can be viewed at wileyonlinelibrary.com.)

results led to a cumulative percent crystallized of 88.2% (Table 3).

Experiment H168 contained olivine, plagioclase, pyroxene, ilmenite, silica, merrillite, and two immiscible liquids, one iron-enriched (Lfe) and one silica-enriched (Lsi). The single observed crystal of olivine was very fayalitic, at Fa_{89} , and the plagioclase compositions increased in anorthite content relative to the J157 experiment, with compositions ranging from An_{67} to An_{73} , with $Or_{1.5-2.7}$. Pyroxenes were zoned and had compositions ranging from $En_{25}Fs_{35}Wo_{40}$ to $En_{18}Fs_{68}Wo_{14}$. Merrillite in this experiment had an approximate formula of $(Mg,Fe,Mn)_{2.68}Ca_{18.04}Na_{0.09}(P,Si)_{14.08}O_{56}$. This merrillite composition lacks a REE component because they were not included in the experiment, and is very iron-rich (6.2 wt% FeO) but is within the range of some lunar merrillite compositions reported in prior work (Jolliff et al., 2006; Joy et al., 2011; Neal & Taylor, 1991). The two liquids, Lfe and Lsi, comprise 12.4 and 21.2%, respectively, of the experiment, according to our LIME calculations. The Lfe is enriched in Ti, Fe, Mn, Mg, Ca, P, and Zr relative to Lsi. Ba partitions roughly equally between the liquids (0.54 and 0.42 wt% BaO in Lfe and Lsi, respectively). Chromium is not found in

detectable amounts in either liquid. The cumulative percentage crystallized after this experiment is 95.8% (Table 3).

The final experiment, J146, contained fayalitic olivine, plagioclase, pyroxene, ilmenite, silica, merrillite, baddeleyite, Lfe, and Lsi. The olivine became significantly more fayalitic at approximately Fa_{95} , from Fa_{89} in H168, and formed intergrowths with Lsi in all occurrences (Fig. 6e). Plagioclase compositions ranged from An_{64} to An_{73} , with orthoclase components continuing to increase ($Or_{2.4-4}$). Pyroxene compositions were strongly and sharply zoned, with cores having a composition of $En_{24}Fs_{54}Wo_{22}$, becoming more calcic to $En_{22}Fs_{50}Wo_{28}$, and very Fe-rich rims of $En_8Fs_{70}Wo_{22}$ at the outer most part (Fig. 7). Merrillite in this experiment had an approximate formula of $(Mg,Fe,Mn)_{2.62}Ca_{18.03}Na_{0.07}(P,Si)_{14.11}O_{56}$. As with the previous experiment, this composition is strongly enriched in FeO similar to merrillite in some other lunar basalts. Lfe and Lsi compositions further diverged with the elements concentrated in Lfe becoming increasingly enriched in Lfe, and elements in Lsi concentrating in Lsi (Fig. 8). Barium was the exception with J146 becoming slightly more concentrated in Lsi than Lfe (0.83 wt% BaO in Lfe and 0.88 wt% BaO in Lsi),

Table 6. Composition of phases in experiments. Full data and uncertainties in Tables S20–S25.

Experiment	Phase	Number of analyses	Beam diameter (μm)	Mean composition in wt%														Total
				SiO ₂	TiO ₂	Al ₂ O ₃	Cr ₂ O ₃	FeO	MnO	MgO	CaO	BaO	Na ₂ O	K ₂ O	P ₂ O ₅	ZrO ₂		
H028	olv	6	1–2	35.53	0.15	n.d.	0.11	37.74	0.37	25.63	0.45	n.i.	n.d.	n.d.	n.d.	n.i.	99.98	
	plag	6	1–2	48.15	0.18	33.02	n.d.	1.09	n.d.	0.29	16.79	n.i.	1.75	0.09	n.d.	n.i.	101.36	
	pyx	5	1	47.96	3.16	4.27	0.37	13.37	0.24	14.09	15.89	n.i.	0.11	n.d.	0.16	n.i.	99.62	
	sp	1	1	n.d.	19.08	6.12	21.79	43.24	0.33	4.14	0.43	n.i.	n.d.	n.d.	n.d.	n.i.	95.13	
	liq	15	10	44.58	5.61	10.06	0.10	20.89	0.24	4.74	10.97	n.i.	0.71	0.25	0.49	n.i.	98.64	
J024	olv	5	3	31.55	0.42	n.d.	n.d.	55.54	0.53	10.51	0.67	n.i.	n.d.	n.d.	n.d.	n.i.	99.22	
	plag	8	3	50.53	0.31	28.66	n.d.	2.29	n.d.	0.44	14.22	n.i.	2.80	0.25	n.d.	n.i.	99.50	
	pyx	14	3	47.97	1.85	1.83	0.21	23.21	0.34	9.29	13.96	n.i.	0.07	0.01	0.01	n.i.	98.75	
	ilm	5	3	n.d.	51.57	0.13	0.50	43.64	0.33	1.68	0.40	n.i.	n.d.	n.d.	n.d.	n.i.	98.25	
	liq	14	3	49.97	3.48	9.48	n.d.	21.64	0.23	1.62	8.82	n.i.	1.03	0.92	0.27	n.i.	97.46	
J157	plag	8	1–5	54.26	0.07	28.61	n.d.	0.83	n.d.	0.10	12.25	0.08	4.16	0.24	0.04	n.d.	100.64	
	pyx	18	1	48.54	1.40	1.60	0.24	25.80	0.40	8.30	13.15	n.d.	0.09	n.d.	n.d.	n.d.	99.53	
	ilm	7	1	0.11	52.76	0.15	0.44	44.59	0.40	1.51	0.17	n.d.	n.d.	n.d.	n.d.	0.10	100.23	
	sil	8	1–5	98.30	0.39	0.97	n.d.	0.48	0.01	n.d.	0.09	0.04	0.27	0.12	n.d.	n.d.	100.68	
	liq	166	1–5	50.15	3.58	9.48	n.d.	21.22	0.27	1.50	8.95	0.26	1.30	0.71	1.08	0.29	98.79	
H168	olv	2	1	29.50	0.12	0.03	n.d.	62.47	0.85	4.46	0.67	n.d.	n.d.	n.d.	0.40	n.d.	98.50	
	plag	36	5	51.24	0.09	29.58	n.d.	1.24	n.d.	0.10	13.71	0.13	3.00	0.40	0.06	n.d.	99.55	
	pyx	17	1	46.67	1.69	1.88	0.11	27.34	0.49	6.58	13.79	n.d.	0.06	n.d.	0.05	0.04	98.72	
	ilm	3	1	0.23	51.53	0.16	0.08	44.62	0.52	0.65	0.28	n.d.	n.d.	n.d.	n.d.	0.31	98.38	
	sil	3	5	97.52	0.34	0.94	n.d.	0.46	n.d.	n.d.	0.09	n.d.	0.31	0.30	n.d.	n.d.	99.96	
J146	merr	3	1	0.72	0.09	0.11	n.d.	6.21	0.16	1.32	45.58	n.d.	0.12	0.03	44.05	n.d.	98.38	
	Lfe	22	1–5	46.19	2.61	8.49	n.d.	24.85	0.39	0.81	9.22	0.54	0.70	1.27	2.51	0.67	98.25	
	Lsi	12	5	67.17	0.91	11.48	n.d.	9.14	0.13	0.25	3.67	0.43	1.27	4.40	0.47	0.26	99.57	
	olv	5	1	29.28	0.37	0.12	n.d.	64.23	0.72	1.85	0.89	0.06	0.03	0.10	0.61	n.d.	98.26	
	plag	24	5	51.88	0.08	28.94	n.d.	1.43	n.d.	0.07	13.43	0.16	3.04	0.46	0.08	n.d.	99.57	
J146	pyx	21	1	45.96	1.56	2.06	0.10	32.75	0.45	4.67	11.14	n.d.	0.05	n.d.	0.04	0.04	98.83	
	ilm	4	1	0.27	50.67	0.11	0.06	45.08	0.39	0.33	0.23	n.d.	n.d.	n.d.	n.d.	0.73	97.86	
	sil	4	1–5	97.45	0.30	1.04	n.d.	0.49	n.d.	n.d.	0.18	n.d.	0.25	0.24	n.d.	n.d.	99.95	
	merr	9	1	1.49	0.11	0.24	n.d.	7.06	0.14	0.78	45.03	0.03	0.12	0.14	43.96	n.d.	99.10	
	Lfe	7	5	44.35	2.51	7.75	n.d.	26.09	0.32	0.40	9.97	0.94	0.52	1.09	2.91	1.42	98.27	
J146	Lsi	12	5	68.59	0.79	11.35	n.d.	7.62	0.08	0.10	3.29	0.88	1.06	4.82	0.37	0.53	99.49	

olv = olivine; plag = plagioclase feldspar; pyx = pyroxene; sp = spinel; ilm = ilmenite; sil = silica; merr = merrillite; liq = liquid; Lfe = iron-enriched liquid; Lsi = silica-enriched liquid; n.d. = not detected; n.i. = not included in composition.

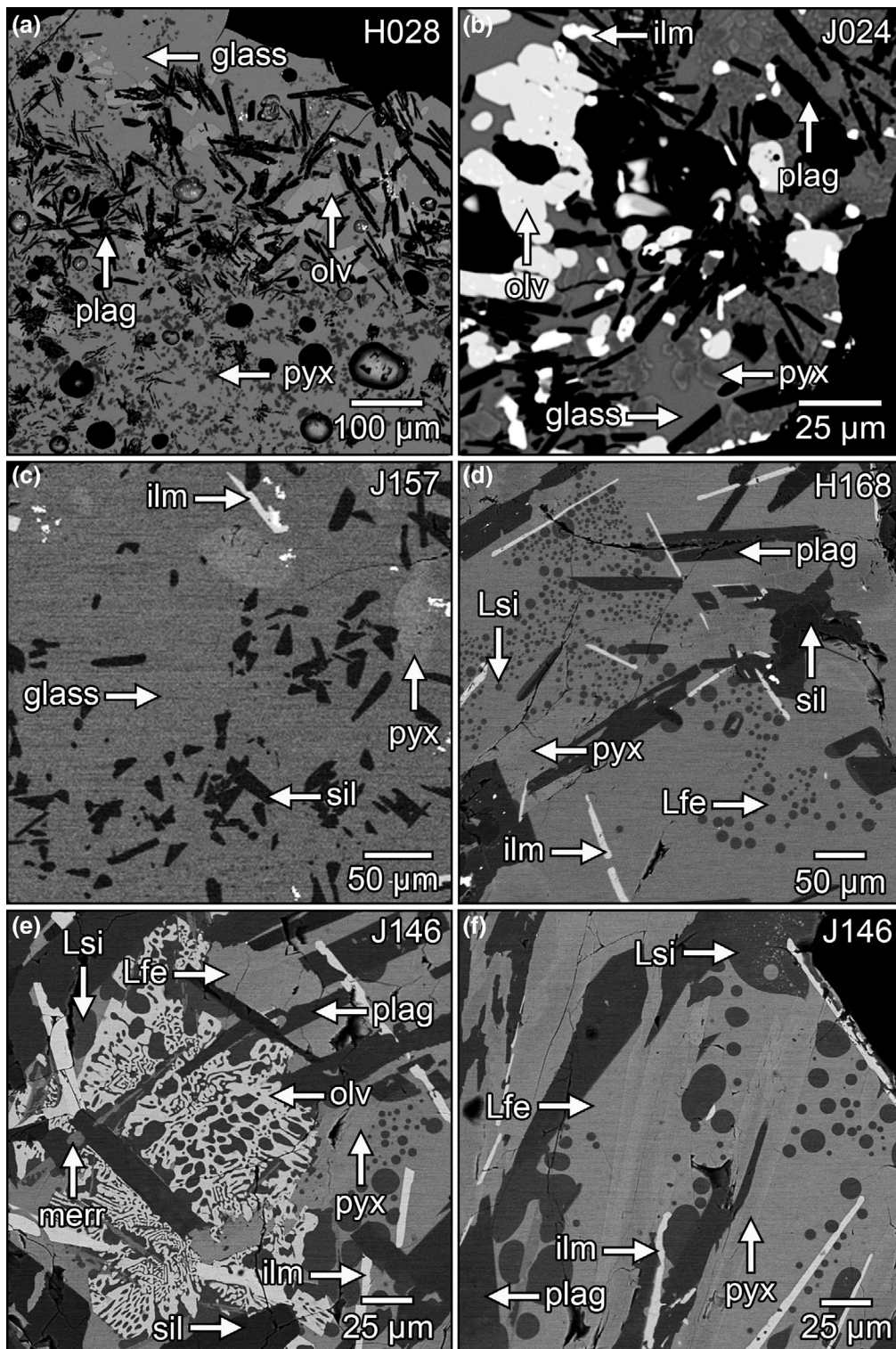


Fig. 6. BSE images of the five experimental charges: (a) H028, (b) J024, (c) J157, (d) H168, (e) J146, (f) J146. Note the change in scale bar between panels. olv = olivine; plag = plagioclase; pyx = pyroxene; glass = non-crystalline residual liquid; ilm = ilmenite; sil = silica; Lsi = silica-enriched liquid; Lfe = iron-enriched liquid; merr = merrillite.

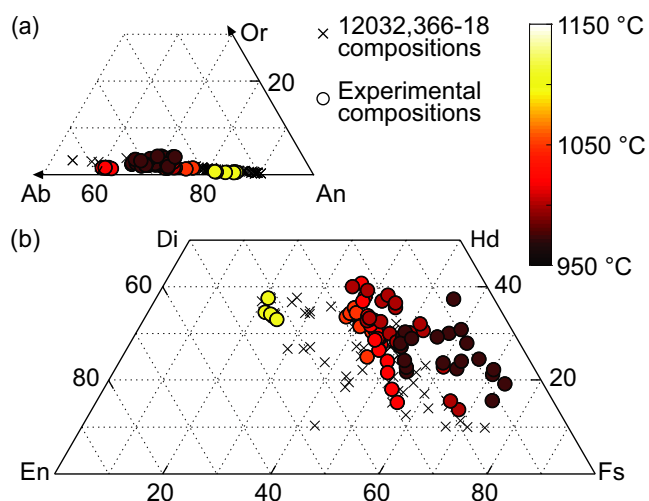


Fig. 7. a) Truncated feldspar ternary diagram, showing variation in 12032,366-18 plagioclase composition, and experimental compositions, color-coded with the final temperature of the experiment. b) Pyroxene quadrilateral, showing variation in 12032,366-18 pyroxene composition, and experimental compositions, color-coded with the final temperature of the experiment. Or = orthoclase; Ab = albite; An = anorthite; Di = diopside; Hd = hedenbergite; En = enstatite; Fs = ferrosilite. (Color figure can be viewed at wileyonlinelibrary.com.)

which was the opposite of what was observed in H168. The overall percent crystallized after J146 was 97.7%.

DISCUSSION

We characterized and determined the bulk composition of basalt fragment 12032,366-18, and experimentally investigated the crystallization history of a melt with similar basaltic composition. Following a brief discussion of the importance of SLI in lunar rocks, we explore how both the experimental basalt and natural lunar basalt crystallized, including how the residual melt evolved during crystallization and its effect on the incompatible-element enrichment of the residual liquids in these basalts. We will also discuss the bulk chemistry of the 12032,366-18, its uniqueness to the Apollo 12 site, and its potential significance as a piece of basaltic material potentially sourced from western Oceanus Procellarum.

Silicate Liquid Immiscibility in Lunar Igneous Rocks

Immiscibility in lunar mare basalt mesostasis represents a late stage process, occurring when the system reaches >85–95% crystallization and when accessory minerals begin to form (Pernet-Fisher et al., 2014; Potts et al., 2016; Roedder & Weiblen, 1977).

Prior to the 1950s, SLI had been discredited as the explanation for the development of layered intrusions on Earth (Bowen, 1928; Harker, 1916), and was found only to occur experimentally at high temperatures (>1500 °C) within geologically improbable melt compositions (e.g., within the binary $\text{SiO}_2\text{--FeO}$ system). However, Roedder (1951) found an immiscibility field at significantly lower temperatures (~1100 °C) in a composition space that was geologically realistic ($\text{K}_2\text{O--FeO--Al}_2\text{O}_3\text{--SiO}_2$). Following Roedder's discovery, there was renewed interest in SLI, both experimentally and in limited terrestrial samples (e.g., De, 1974; Ferguson & Currie, 1972; Philpotts, 1971).

After the return of lunar mare basalt samples from the Apollo program, petrographic studies of mesostasis regions in these samples revealed evidence of immiscibility between a felsic and basaltic liquid (Roedder & Weiblen, 1970). Since then, SLI has been observed or inferred in a multitude of mare basalt mesostasis (e.g., Day et al., 2006; Hess et al., 1975; Pernet-Fisher et al., 2014; Potts et al., 2016; Roedder & Weiblen, 1977; Rutherford et al., 1974).

The mineral apatite is used as an indicator of volatile content in parent magmas (Barnes et al., 2014; Boyce et al., 2010; McCubbin et al., 2011; Tartèse et al., 2014). Apatite crystallizes late in the solidification of a magma (e.g., Sha, 2000) and is commonly found in late-stage mesostasis areas, some of which show evidence for SLI (e.g., Potts et al., 2016). Therefore, the timing of the onset of immiscibility relative to the formation of accessory minerals such as apatite is important and necessary to fully understand the geochemical environment and processes by which these minerals formed (e.g., Hallis et al., 2014; Longhi, 1992; Potts et al., 2016).

12032,366-18 in the Context of the Cooling Experiments

As mineral phases became thermodynamically favored at different temperatures, we observed that the composition of the residual liquid, or glass, changed correspondingly (Fig. 8a), an effect that has been observed in petrologic experiments (e.g., Longhi, 1992; Toplis et al., 1994), demonstrated via chemical modeling (e.g., Hallis et al., 2014) and inferred from lunar basalts (e.g., Neal et al., 1988; Potts et al., 2016). When the residual liquid changes composition, so does the chemistry of the crystallizing phases (e.g., Hallis et al., 2014). We observed this change in mineral chemistry in both the cooling experiments and the petrology of 12032,366-18, and directly observed the change in residual liquid (glass) composition during cooling in the experiments (Table 6; Figs. 9 and 10). The temperature range over which crystallizing occurs, and the system's overall percent crystallized at a given temperature

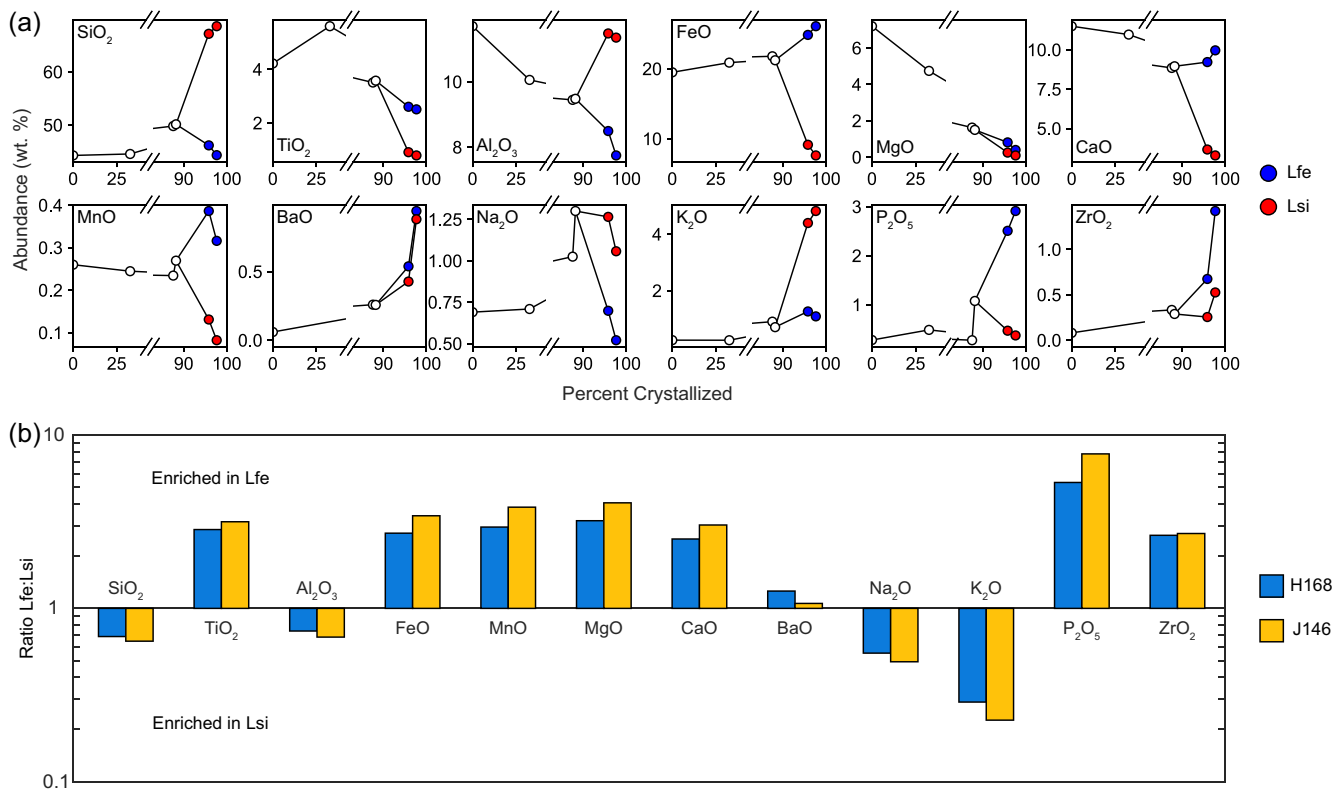


Fig. 8. a) Abundance of each oxide in the residual liquid (glass) as a function of percent crystallized. Note the break and change in scale on bottom axes. Red dots represent Lsi, blue dots represent Lfe. See the text for discussion. b) Ratio of Lfe to Lsi for each oxide, in the H168 (blue) and J146 (yellow) experiments. Values greater than one indicate greater concentration in Lfe, values less than one indicate greater concentration in Lsi. (Color figure can be viewed at wileyonlinelibrary.com.)

(Table 3), is most consistent with low-Ti mare basalts (Fagan et al., 2014).

The observed trends in olivine, plagioclase, and pyroxene chemistry in the experiments overlap with and are consistent with that of 12032,366-18. Olivine appears to be in a resorption reaction with pyroxene in 12032,366-18 (Fig. 4d), which is consistent with the disappearance of intermediate composition olivine (approximately Fo₅₅₋₂₀) in the J157 experiment. Plagioclase in 12032,366-18 ranges from approximately An₉₀ to An₅₅, but the experiments have a narrower compositional range from An₈₇ to An₆₀. A key difference in plagioclase between the sample and experiments is the reversal of the decreasing An content trend between the J157 and H168 experiments, whereas 12032,366-18 shows a continual decrease of the An component approaching mesostasis regions. The cause for the reversal in An content in the experiments remains unknown. Pyroxene compositions trend more calcic with increasing crystallinity of the system. Prior to the onset of SLI (experiments H028, J024, and J157), the enstatite content of pyroxene was approximately constant in a given experiment, with zoning occurring between Ca and Fe. Progressive experiments saw the

enstatite component drop from ~42 to ~25. In H168 and J146, pyroxenes begin to show strong zoning toward the Fe-endmember, similar to many Fe-rich rims found approaching mare basalt mesostasis (e.g., Anand et al., 2006; Liu et al., 2009; Potts et al., 2016) and observed in 12032,366-18. The zoning in J146 pyroxenes is sharp in some instances. This change in pyroxene chemistry also initially appears in the same experiment that shows SLI (H168).

The crystallization sequence is similar in 12032,366-18 and the experiments to many low-Ti mare basalts. We do however observe plagioclase in our highest temperature experiment, which is not expected to crystallize early in low-Ti basalts (Lucey et al., 2006). The bulk major element composition of 12032,366-18 is similar to that of Apollo 12 pigeonite basalt 12064 and Apollo 12 ilmenite basalt 12051, except that Na₂O, K₂O, P₂O₅, and the incompatible trace elements are all a factor of ~3 higher in 12032,366-18 (Wieczorek et al. [2006] and references therein). The presence of olivine in both 12032,366-18 and the experiments suggests that this sample is not closely related to KREEP basalts, which typically do not contain olivine (e.g., Fagan et al., 2014; Takeda et al., 1978). Additionally, KREEP

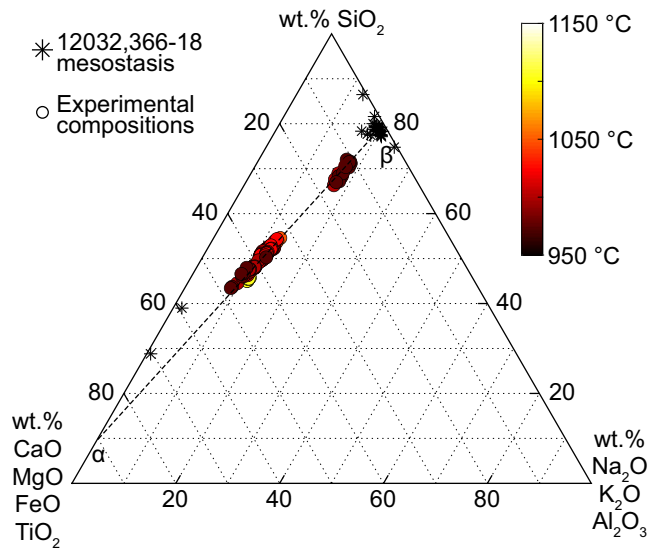


Fig. 9. Pseudoternary with axes of SiO_2 at top; $\text{CaO} + \text{MgO} + \text{FeO} + \text{TiO}_2$ at left; and $\text{Na}_2\text{O} + \text{K}_2\text{O} + \text{Al}_2\text{O}_3$ at right, showing the composition of the bulk mesostases from 12032,366-18, as determined by defocused beam analyses (Table 2), and glasses from experimental charges, color-coded with the final temperature of the experiment. Line α - β is defined by endpoints (10%, 90%, 0%) and (80%, 0%, 20%), and is used in Fig. 10, where all data points are projected onto this line. (Color figure can be viewed at wileyonlinelibrary.com.)

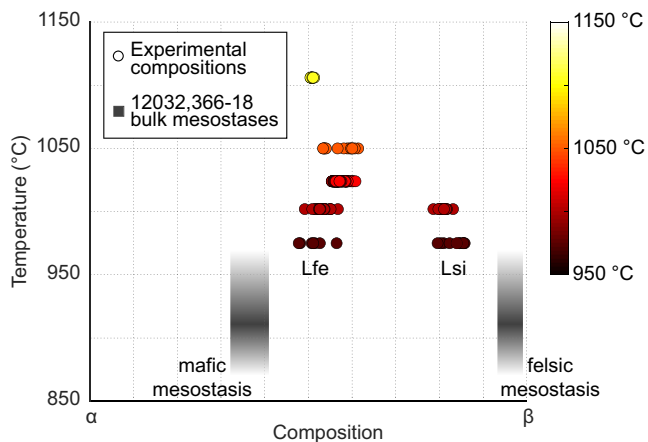


Fig. 10. Plot showing final temperature of experimental glasses projected onto the compositional line α - β from Fig. 9. The composition of 12032,366-18 mesostases, projected onto the line α - β , are not at a defined temperature, and are plotted as gradational gray boxes. The gradation is darkest where we expect the experimental liquids to intersect with the sample's compositions. Lfe = iron-enriched liquid; Lsi = silica-enriched liquid. (Color figure can be viewed at wileyonlinelibrary.com.)

basalts have pyroxene with higher enstatite content than our sample and experiments.

As the experimental residual liquid evolves, it becomes enriched in incompatible elements such as Ba,

Na, K, P, and Zr, as is expected for a mare basalt composition under lunar-like conditions (e.g., Hallis et al., 2014; Potts et al., 2016). With the onset of SLI between the J157 and H168 experiments, which had final temperatures of 1024 and 1002 °C, respectively, elements partition between Lfe and Lsi in a predictable manner (Figs. 8–10). In 12032,366-18, and in typical lunar mare basalts, we observe mesostasis regions enriched in Si, Al, Na, K, and Ba. This behavior is the same as that in our experiments, except for barium, for which the concentration in Lsi and Lfe are within error of each other (Fig. 8). The partitioning behavior of Ba is known to depend on the concentration of K and Na in Lsi (Neal & Taylor, 1989).

In the petrologic experiments, intergrowths of fayalite and Lsi occur along with regions of Lsi blebs in Lfe matrix, in our lowest temperature experiment. In 12032,366-18, the mesostasis regions do not appear as intergrowths with fayalite, although Si-K-rich glass intergrowths with fayalite are seen in some examples of lunar mesostasis (Potts et al., 2016). Mineral assemblages in the low-temperature experiments (merrillite, baddeleyite, silica, and fayalite) are similar in composition to those of mesostasis regions in 12032,366-18. Troilite was observed in 12032,366-18, but not found in our experiments because our experimental compositions did not include sulfur. Similarly, apatite and RE-merrillite were not found in the experiments due to the constrained compositions (lack of REEs, F, Cl, OH) of our starting material, but are represented by merrillite. Barian K-feldspar was also not observed in our experiments, possibly because the experiments concluded at 975 °C, somewhat above the system's solidus, which we expect between 900 and 950 °C (Fig. 10).

Is 12032,366-18 Unique Among the Lunar Mare Basalt Collection?

To facilitate comparison of the bulk composition of 12032,366-18 to Apollo 12, and other lunar basalt suites, it is critical to determine if the bulk composition is representative of a liquid. One way to assess the reliability of the bulk composition of the rock as a liquid composition is to compare the bulk rock $\text{Mg}\#$ to the forsterite content of the most primitive olivine (Roeder & Emslie, 1970; Snape et al., 2014). Unfortunately, the most primitive olivine in the analyzed section of 12032,366-18 has a composition of Fo_{38} , which is insufficiently primitive to obtain a bulk rock $\text{Mg}\#$ comparable to the sample's $\text{Mg}\#$ of 39.7. This test, therefore, is inconclusive in determining if the bulk composition of the sample is representative of a liquid.

However, as we describe in the 12032,366-18 in the Context of the Cooling Experiments section, the mineral chemistry in the experiments match that of 12032,366-18. Based on the chemistry of observed minerals, as well as the sequence of crystallization, in the experiments, we conclude that the calculated bulk composition of 12032,366-18 is representative of a bulk liquid that crystallized as a relatively closed system.

Several other studies have investigated Apollo 12 soils in search of chemically distinct basaltic soil fragments (Alexander et al., 2014, 2016; Snape et al., 2014). The potentially unique basalts identified in these studies are each dissimilar to 12032,366-18 in mineral chemistry, bulk composition, and texture. Therefore, we conclude that 12032,366-18 represents a previously undescribed lithology likely foreign to the Apollo 12 site.

Major basalt groups from Luna and other Apollo sites are also dissimilar to 12032,366-18, which contain different amounts of TiO_2 , Al_2O_3 , or K_2O . The most similar in bulk composition are Apollo 14, 15, and Luna 16 basalts (Neal & Taylor, 1992). Apollo 14 basalts consist of “high Al” and “very high K” or VHK groups. The high-Al group have similar K abundances, but typically lower TiO_2 (~2–3 wt%). The VHK basalts from Apollo 14 contain, as expected by their name, significantly higher K than 12032,366-18 on average. Apollo 15 pigeonite and olivine basalts both contain less TiO_2 (<3 wt%) than our sample. Luna 16 basalts contain slightly more Al_2O_3 than 12032,366-18 (~13 wt % versus 11.7 wt%) and slightly higher TiO_2 (Taylor et al., 1991).

Apollo 12 basalts consistently contain less than 2 ppm bulk Th (Taylor et al., 1991), with one exception, olivine mare basalt 12018 (Bouchet et al., 1971), for which 12018,43 contains 3.3 ppm Th, determined by alpha autoradiography with ~250 mg of material. Other studies examining different splits of 12018 observed lower (<2 ppm) bulk Th values (Brunfelt et al., 1971; Goles et al., 1971; Wänke et al., 1971), all of which used INAA and 0.5–1.0 g of material. Unfortunately, bulk-rock Th contents for the samples studied by Snape et al. (2014) and Alexander et al. (2014, 2016) were not reported, and thus comparison is not feasible. Based on the trace element-rich nature of 12032,366-18 reported here, this basalt fragment remains anomalous among Apollo 12 basalt samples.

Other mare basalt groups also consistently have low bulk Th, always falling under 5 ppm, and most falling under 3 ppm (Fig. 3). Exceptions to this include a recently returned Chang'E 5 basalt fragment (Tian et al., 2021), and Apollo 11 high-K basalts (Wieczorek et al., 2006). Apollo 15 KREEP basalts have more than

10 ppm Th, and Apollo 17 KREEP basalts, ~4–8 ppm Th. However, as noted in the Characterization of 12032,366-18 section, these two suites contain significantly less FeO and TiO_2 than our sample 12032,366-18 (Fig. 3).

The minor and trace element composition and the high Th content of 12032,366-18 are anomalous relative to other basalts. Combined, these two findings indicate that 12032,366-18 represents a unique basalt not previously identified at the Apollo 12 landing site. Using results from Barra et al. (2006), we can further state that the young “minimum age” inferred for 12032,366-18 (2.3 Ga) is unusual for Apollo 12 basalts, where the youngest unit is ~3.1 Ga (Snape et al., 2018). We propose that 12032,366-18 is foreign to the Apollo 12 landing site, delivered by impact, given its chemistry, petrology, and minimum ^{40}Ar - ^{39}Ar systematics, including possible disturbance circa 500–700 Ma (see below).

Trace element-enriched magmas on the Moon can originate from several different processes, including assimilation of various crustal and mantle components, fractional crystallization, or metasomatism. These various processes are typically discerned by observing trends in bulk or mineral compositional data from basalts of the same group in various element abundance or ratio plots (e.g., Hallis et al., 2014; Neal & Taylor, 1992), where these processes produce distinct elemental trends. For 12032,366-18, we are unable to perform such analyses. This sample is unique, and thus only plots as a single point on any element abundance or ratio plot, which inherently has no trend. Should more basalts of this type be recognized in the lunar sample collection, it may be possible to then discern a trend, and therefore, also a method of trace element enrichment.

Geographical Origin of Basalt 12032,366-18

Thorium-enriched mare basalts have been detected remotely in western Oceanus Procellarum via the gamma-ray spectrometer on Lunar Prospector (Lawrence et al., 1998, 2003, 2007; Prettyman et al., 2006). While adjacent to two Th “hot spots” at Kepler crater (~12 ppm Th) and the Aristarchus crater and plateau (~15 ppm Th), there are also mare basalts with Th contents apparently ranging from 5 to 8 ppm in western Oceanus Procellarum (Fig. 11), higher than the Th content for Apollo 12 basalts. There are regions in Oceanus Procellarum that broadly have similar FeO and Ti contents as 12032,366-18, as determined by remote sensing. However, the spatial resolution varies between these maps and, for the Ti Lunar Prospector map, it has a resolution of 2° per pixel (Prettyman et al., 2006).

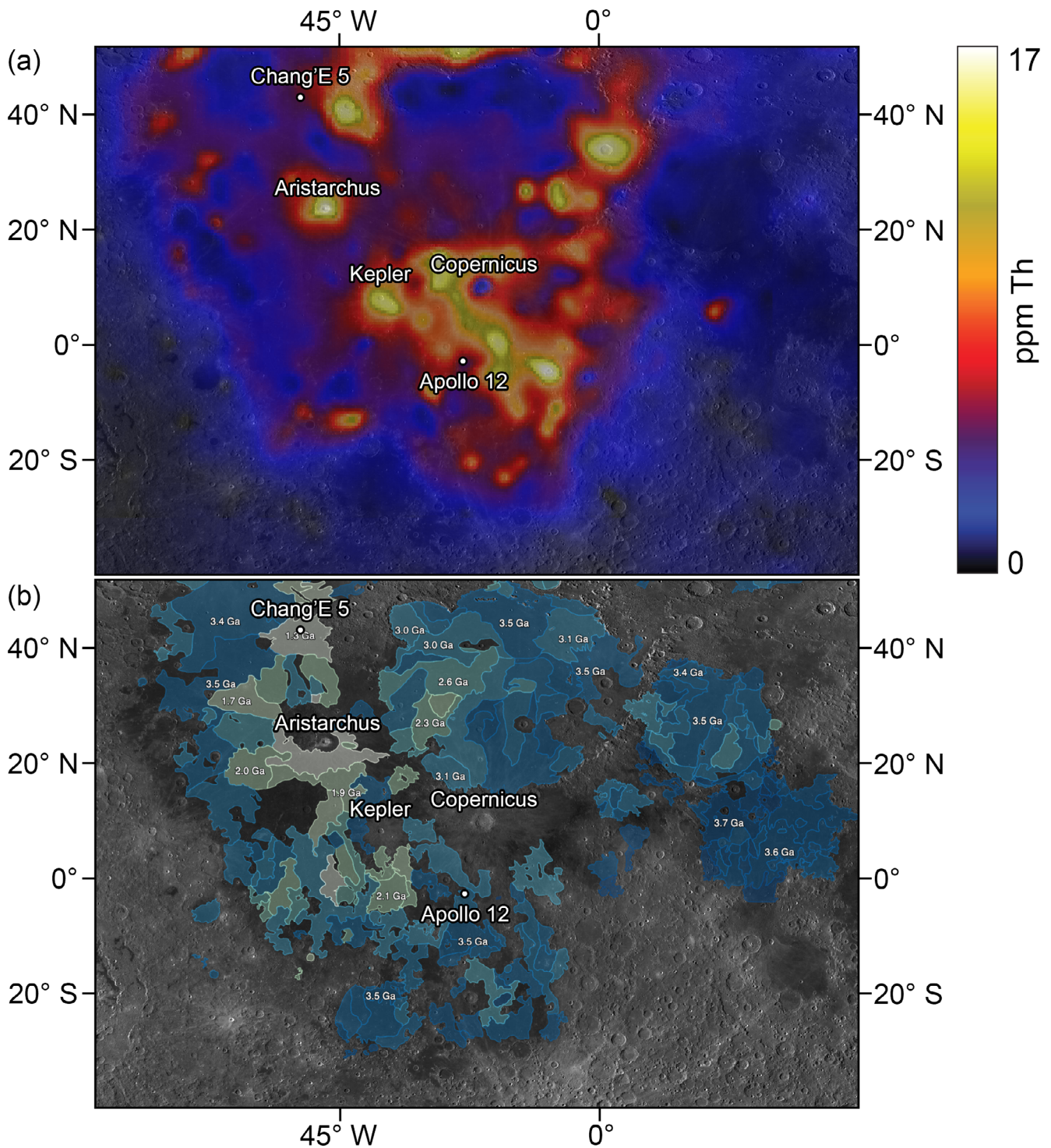


Fig. 11. a) Thorium abundance map of a portion of the lunar nearside. Data from Lawrence et al. (2007). b) Age of mare basalts, where darkest blues represent older ages up to 4 Ga and white represents younger ages down to 1.2 Ga. Data from Hiesinger et al. (2011). Both images were acquired via the Lunar QuickMap: quickmap.lroc.asu.edu. Basemap credit to NASA/GSFC/Arizona State University. (Color figure can be viewed at wileyonlinelibrary.com.)

Western Oceanus Procellarum is also known for its geologically young mare basalts, with ages as young as 1 Ga, as determined via crater counting (Hiesinger et al.,

2003; Qian et al., 2018; Stadermann et al., 2018). Many (>10) units in this region have been dated at less than 3 Ga by crater counting (Hiesinger et al., 2003). These

moderately young (2–3 Ga) lava flows coincide with the regions moderately enriched in Th (5–8 ppm) and may be the source region for the Th-enriched 12032,366-18, which has a young minimum crystallization age. Recently, samples from this part of the Moon were returned to Earth via the Chang'E 5 mission. These Chang'E 5 basalts were determined to have an approximate age of 2.0 Ga (Che et al., 2021; Li et al., 2021).

Impact events redistribute material on the Moon's surface, which enabled the Apollo astronauts to retrieve a great variety of lithologies from only six landing sites. It is expected, therefore, that a portion of the material collected at any given landing site was delivered there via impact redistribution and is thus foreign to that locale. Barra et al. (2006) found that 12032,366-18 exhibited multiple degassing ages. The disturbance age of 500–700 Ma for 12032,366-18 was plausibly caused by an impact event that delivered the rock fragment to the Apollo 12 landing site. The Apollo 12 site is located on a crater ray of Copernicus, and a significant portion of the Apollo 12 samples have disturbance ages of ~800 Ma, which is inferred to be the age of the Copernicus impact event (Bogard et al., 1994). The 500–700 Ma age for 12032,366-18 is distinct from this Copernican event (Barra et al., 2006), but other large, young craters in the region may be plausible origins for this sample. Kepler crater, located 550 km northwest of the Apollo 12 landing site, could be a viable candidate source crater and has age estimates of 625–950 Ma (König et al., 1977) and 780 Ma (McEwen et al., 1993). Apollo sample 12032,366-18 is a compositionally distinct, potentially young basalt fragment, unlike other Apollo 12 basalts and unlike other characterized Apollo 12 basaltic soil fragments. 12032,366-18 is enriched in thorium (7 ppm Th), as well as other incompatible minor and trace elements. The sample gives a young minimum crystallization age of 2.3 Ga, with a disturbance age between 500 and 700 Ma (Barra et al., 2006). These attributes indicate that 12032,366-18 is foreign to the Apollo 12 landing site and is potentially representative of a mare basalt from western Oceanus Procellarum.

CONCLUSIONS

We characterized the petrography and geochemistry of sample 12032,366-18 and performed petrologic experiments that reproduce the crystallization sequence of this basalt fragment. Using these approaches, we have arrived at several conclusions.

1. The bulk composition of 12032,366-18 may represent liquid composition, despite the fragment's small size.
2. The mesostasis regions in 12032,366-18 likely formed via SLI, onsetting between 1030 and

1002 °C. Phosphate saturation also occurred in this temperature range. SLI has been inferred in numerous lunar samples and experimental work has shown that lunar-like compositions experience SLI, but only a few studies that have investigated a sample's crystallization sequence and SLI occurrence using petrologic experiments.

3. 12032,366-18 is likely foreign to the Apollo 12 landing site judging by its young minimum crystallization age and enrichment in incompatible trace elements such as thorium. These attributes, in addition to a degassing age at 500–700 Ma (Barra et al., 2006), indicate that 12032,366-18 may have arrived at the Apollo 12 site as impact ejecta from elsewhere in the region, likely from a large, young crater such as Kepler that is known to have struck a mare basalt target. An updated model age for Kepler via crater counting would help in identifying if the Kepler crater could have been the source region for 12032,366-18.

Continued characterization of Apollo and Luna soil fragments may discover more unique mare basalt fragments, which would broaden the known diversity of basalts on the Moon. In addition to samples from Chang'E 5, future landed and sample return missions to unexplored regions of nearside mare basalts may support the finding that 12032,366-18 is from a young, Th-enriched flow in that area. Expanding the known diversity of basaltic compositions on the Moon would help constrain the thermal and magmatic evolution of the Moon.

Acknowledgments—We thank NASA for the loan of Apollo sample 12032,366. We thank Paul Carpenter, Ken Domanik, Hélène Couvy Craigg, and Kelsey Prissel for their help with this study. We thank Dr. Steve Elardo and Dr. Joshua Snape, as well as associate editor Dr. Katherine Joy, for their helpful comments that have significantly improved this paper. We acknowledge the support of the McDonnell Center for the Space Sciences for the EPMA studies. We acknowledge the use of imagery from Lunar QuickMap (quickmap.lroc.asu.edu), a collaboration between NASA, Arizona State University, and Applied Coherent Technology Corp. This study was supported by NASA grants NNX14AI65G (BLJ), 80NSSC20K0640 (MJK), NNX15AL60G (ACS and CWH), and 80NSSC19K0871 (CWH). JJB and ACS were supported by start-up funds from the University of Arizona.

Data Availability Statement—All data available in supporting information files.

Editorial Handling—Dr. Katherine Joy

REFERENCES

- Alexander, L., Snape, J. F., Crawford, I. A., Joy, K. H., and Downes, H. 2014. Searching for Nonlocal Lithologies in the Apollo 12 Regolith: A Geochemical and Petrological Study of Basaltic Coarse Fines from the Apollo Lunar Soil Sample 12023,155. *Meteoritics & Planetary Science* 49: 1288–304.
- Alexander, L., Snape, J. F., Joy, K. H., Downes, H., and Crawford, I. A. 2016. An Analysis of Apollo Lunar Soil Samples 12070,889, 12030,187, and 12070,891: Basaltic Diversity at the Apollo 12 Landing Site and Implications for Classification of Small-Sized Lunar Samples. *Meteoritics & Planetary Science* 51: 1654–77.
- Anand, M., Taylor, L. A., Floss, C., Neal, C. R., Terada, K., and Tanikawa, S. 2006. Petrology and Geochemistry of LaPaz Icefield 02205: A New Unique Low-Ti Mare-Basalt Meteorite. *Geochimica et Cosmochimica Acta* 70: 246–64.
- Barnes, J. J., Tartèse, R., Anand, M., McCubbin, F. M., Franchi, I. A., Starkey, N. A., and Russell, S. S. 2014. The Origin of Water in the Primitive Moon as Revealed by the Lunar Highlands Samples. *Earth and Planetary Science Letters* 390: 244–52.
- Barra, F., Swindle, T. D., Korotev, R. L., Jolliff, B. L., Zeigler, R. A., and Olson, E. 2006. $^{40}\text{Ar}/^{39}\text{Ar}$ Dating of Apollo 12 Regolith: Implications for the Age of Copernicus and the Source of Nonmare Materials. *Geochimica et Cosmochimica Acta* 70: 6016–31.
- Bogard, D. D., Garrison, D. H., Shih, C. Y., and Nyquist, L. E. 1994. ^{39}Ar - ^{40}Ar Dating of Two Lunar Granites: The Age of Copernicus. *Geochimica et Cosmochimica Acta* 58: 3093–100.
- Bouchet, M., Kaplan, G., Voudon, A., and Bertolotti, M.-J. 1971. Spark Mass Spectrometric Analysis of Major and Minor Elements in Six Lunar Samples. Proceedings, 2nd Lunar Science Conference. p. 1247.
- Bowen, N. L. 1928. *The Evolution of the Igneous Rocks*. Princeton, NJ: Princeton University Press. 332 p.
- Boyce, J. W., Liu, Y., Rossman, G. R., Guan, Y., Eiler, J. M., Stolper, E. M., and Taylor, L. A. 2010. Lunar Apatite with Terrestrial Volatile Abundances. *Nature* 466: 466–9.
- Brunfelt, A. O., Heier, K. S., and Steinnes, E. 1971. Determination of 40 Elements in Apollo 12 Materials by Neutron Activation Analysis. Proceedings, 2nd Lunar Science Conference. p. 1281.
- Che, X., Nemchin, A., Liu, D., Long, T., Wang, C., Norman, M. D., Joy, K. H. et al. 2021. Age and Composition of Young Basalts on the Moon, Measured from Samples Returned by Chang'e-5. *Science* 374: eabl7957.
- Day, J. M. D. D., Taylor, L. A., Floss, C., Patchen, A. D., Schnare, D. W., and Pearson, D. G. 2006. Comparative Petrology, Geochemistry, and Petrogenesis of Evolved, Low-Ti Lunar Mare Basalt Meteorites from the LaPaz Icefield, Antarctica. *Geochimica et Cosmochimica Acta* 70: 1581–600.
- De, A. 1974. Silicate Liquid Immiscibility in the Deccan Traps and Its Petrogenetic Significance. *Geological Society of America Bulletin* 85: 471.
- Fagan, T. J., Kashima, D., Wakabayashi, Y., and Suginothara, A. 2014. Case Study of Magmatic Differentiation Trends on the Moon Based on Lunar Meteorite Northwest Africa 773 and Comparison with Apollo 15 Quartz Monzodiorite. *Geochimica et Cosmochimica Acta* 133: 97–127.
- Ferguson, J., and Currie, K. L. 1972. Silicate Immiscibility in the Ancient “Basalts” of the Barberton Mountain Land, Transvaal. *Nature Physical Science* 235: 86–9.
- Gavrilenko, M., Krawczynski, M., Ruprecht, P., Li, W., and Catalano, J. G. 2019. The Quench Control of Water Estimates in Convergent Margin Magmas. *American Mineralogist* 104: 936–48.
- Gillis, J. J., Jolliff, B. L., and Elphic, R. C. 2003. A Revised Algorithm for Calculating TiO_2 from Clementine UVIS Data: A Synthesis of Rock, Soil, and Remotely Sensed TiO_2 Concentrations. *Journal of Geophysical Research: Planets* 108: 5009.
- Goles, G. G., Duncan, A. R., Lindstrom, D. J., Martin, M. R., Beyer, R. L., Osawa, M., Randle, K., Meek, L. T., Steinborn, T. L., and McKay, S. M. 1971. Analyses of Apollo 12 Specimens: Compositional Variations, Differentiation Processes, and Lunar Soil Mixing Models. Proceedings, 2nd Lunar Science Conference. p. 1063.
- Grove, T. L., Holbig, E. S., Barr, J. A., Till, C. B., and Krawczynski, M. J. 2013. Melts of Garnet Lherzolite: Experiments, Models and Comparison to Melts of Pyroxenite and Carbonated Lherzolite. *Contributions to Mineralogy and Petrology* 166: 887–910.
- Gullikson, A. L., Hagerty, J. J., Reid, M. R., Rapp, J. F., and Draper, D. S. 2016. Silicic Lunar Volcanism: Testing the Crustal Melting Model. *American Mineralogist* 101: 2312–21.
- Hallis, L. J., Anand, M., and Strekopytov, S. 2014. Trace-Element Modelling of Mare Basalt Parental Melts: Implications for a Heterogeneous Lunar Mantle. *Geochimica et Cosmochimica Acta* 134: 289–316.
- Harker, A. 1916. Differentiation in Intercrustal Magma Basins. *Journal of Geology* 24: 554–8.
- Hess, P. C., Rutherford, M. J., Guillemette, R. N., Ryerson, F. J., and Tuchfeld, H. A. 1975. Residual Products of Fractional Crystallization of Lunar Magmas: An Experimental Study. Proceedings, 11th Annual Lunar Science Conference. pp. 895–909.
- Hiesinger, H., Head III, J. W., Wolf, U., Jaumann, R., and Neukum, G. 2003. Ages and Stratigraphy of Mare Basalts in Oceanus Procellarum, Mare Nubium, Mare Cognitum, and Mare Insularum. *Journal of Geophysical Research* 108.
- Hiesinger, H., Head III, J. W., Wolf, U., Jaumann, R., and Neukum, G. 2011. Ages and Stratigraphy of Lunar Mare Basalts: A Synthesis. In *Recent Advances and Current Research Issues in Lunar Stratigraphy*, edited by W. A. Ambrose, and D. A. Williams. McLean, Virginia: Geological Society of America.
- Jolliff, B. L., Gillis, J. J., Lawrence, D. J., and Maurice, S. 2001. Thorium Content of Mare Basalts of the Western Procellarum Region (Abstract #2143). 32nd Lunar and Planetary Science Conference. CD-ROM.
- Jolliff, B. L., Hughes, J. M., Freeman, J. J., and Zeigler, R. A. 2006. Crystal Chemistry of Lunar Merrillite and Comparison to Other Meteoritic and Planetary Suites of Whitlockite and Merrillite. *American Mineralogist* 91: 1583–95.
- Jolliff, B. L., Zeigler, R. A., Korotev, R. L., Barra, F., and Swindle, T. D. 2005. A Thorium-Rich Mare Basalt Rock Fragment from the Apollo 12 Regolith: A Sample from a Young Procellarum Flow? (Abstract #2357). 36th Lunar and Planetary Science Conference. CD-ROM.
- Joy, K. H., Burgess, R., Hinton, R., Fernandes, V. A., Crawford, I. A., Kearsley, A. T., and Irving, A. J. 2011. Petrogenesis and Chronology of Lunar Meteorite

- Northwest Africa 4472: A KREEPy Regolith Breccia from the Moon. *Geochimica et Cosmochimica Acta* 75: 2420–52.
- König, B., Neukum, G., and Fechtig, H. 1977. Recent Lunar Cratering: Absolute Ages of Kepler, Aristarchus, Tycho (Abstract). 8th Lunar Science Conference. p. 555.
- Korotev, R. L. 1991. Geochemical Stratigraphy of Two Regolith Cores from the Central Highlands of the Moon. Proceedings, 21st Lunar and Planetary Science Conference. pp. 229–89.
- Korotev, R. L., Jolliff, B. L., Zeigler, R. A., Seddio, S. M., and Haskin, L. A. 2011. Apollo 12 Revisited. *Geochimica et Cosmochimica Acta* 75: 1540–73.
- Kramer, G. Y., and Neal, C. R. 2003. Petrogenesis of the Apollo 14 High-Al Basalts Revisited: Distinct Magmatic Events, Source Metasomatism, and AFC (Abstract #2035). 34th Lunar and Planetary Science Conference. CD-ROM.
- Krawczynski, M. J., and Olive, J. L. 2011. A New Fitting Algorithm for Petrological Mass-Balance Problems. American Geophysical Union, Fall Meeting.
- Lawrence, D. J., Elphic, R. C., Feldman, W. C., Prettyman, T. H., Gasnault, O., and Maurice, S. 2003. Small-Area Thorium Features on the Lunar Surface. *Journal of Geophysical Research: Planets* 108.
- Lawrence, D. J., Feldman, W. C., Barraclough, B. L., Binder, A. B., Elphic, R. C., Maurice, S., Miller, M. C., and Prettyman, T. H. 2000. Thorium Abundances on the Lunar Surface. *Journal of Geophysical Research* 105: 20307–32.
- Lawrence, D. J., Feldman, W. C., Barraclough, B. L., Binder, A. B., Elphic, R. C., Maurice, S., and Thomsen, D. R. 1998. Global Elemental Maps of the Moon: The Lunar Prospector Gamma-Ray Spectrometer. *Science* 281: 1484–89.
- Lawrence, D. J., Feldman, W. C., Elphic, R. C., Little, R. C., Prettyman, T. H., Maurice, S., Lucey, P. G., and Binder, A. B. 2002. Iron Abundances on the Lunar Surface as Measured by the Lunar Prospector Gamma-Ray and Neutron Spectrometers. *Journal of Geophysical Research: Planets* 107: 5130.
- Lawrence, D. J., Puetter, R. C., Elphic, R. C., Feldman, W. C., Hagerty, J. J., Prettyman, T. H., and Spudis, P. D. 2007. Global Spatial Deconvolution of Lunar Prospector Th Abundances. *Geophysical Research Letters* 34.
- Li, Q.-L., Zhou, Q., Liu, Y., Xiao, Z., Lin, Y., Li, J.-H., Ma, H.-X. et al. 2021. Two-Billion-Year-Old Volcanism on the Moon from Chang'e-5 Basalts. *Nature* 600: 54–8.
- Liu, Y., Floss, C., Day, J., James, M., Hill, E., and Taylor, L. 2009. Petrogenesis of Lunar Mare Basalt Meteorite Miller Range 05035. *Meteoritics & Planetary Science* 44: 261–84.
- Longhi, J. 1992. Experimental Petrology and Petrogenesis of Mare Volcanics. *Geochimica et Cosmochimica Acta* 56: 2235–51.
- Lucey, P., Korotev, R. L., Gillis, J. J., Taylor, L. A., Lawrence, D., Campbell, B. A., Elphic, R. et al. 2006. Understanding the Lunar Surface and Space-Moon Interactions. *Reviews in Mineralogy and Geochemistry* 60: 83–219.
- Maloy, A. K., and Treiman, A. H. 2007. Evaluation of Image Classification Routines for Determining Modal Mineralogy of Rocks from X-Ray Maps. *American Mineralogist* 92: 1781–8.
- Marvin, U. B., Wood, J. A., Taylor, G. J., Reid, J. B. J., Powell, B. N., Dickey, J. S. J., and Bower, J. F. 1971. Relative Proportions and Probable Sources of Rock Fragments in the Apollo 12 Soil Samples. Proceedings, 2nd Lunar Science Conference. p. 679.
- McCubbin, F. M., Jolliff, B. L., Nekvasil, H., Carpenter, P. K., Zeigler, R. A., Steele, A., Elardo, S. M., and Lindsley, D. H. 2011. Fluorine and Chlorine Abundances in Lunar Apatite: Implications for Heterogeneous Distributions of Magmatic Volatiles in the Lunar Interior. *Geochimica et Cosmochimica Acta* 75: 5073–93.
- McCubbin, F. M., Vander Kaaden, K. E., Tartèse, R., Klima, R. L., Liu, Y., Mortimer, J., Barnes, J. J. et al. 2015. Magmatic Volatiles (H, C, N, F, S, Cl) in the Lunar Mantle, Crust, and Regolith: Abundances, Distributions, Processes, and Reservoirs. *American Mineralogist* 100: 1668–707.
- McEwen, A. S., Gaddis, L. R., Neukum, G., Hoffman, H., Pieters, C. M., and Head, J. W. 1993. Galileo Observations of Post-Imbrium Lunar Craters During the First Earth-Moon Flyby. *Journal of Geophysical Research: Planets* 98: 17207–31.
- McKay, D. S., Morrison, D. A., Clanton, U. S., Ladle, G. H., and Lindsay, J. F. 1971. Apollo 12 Soil and Breccia. Proceedings, 2nd Lunar Science Conference. p. 755.
- Meyer, C. 2011. *Lunar Sample Compendium*. Houston, Texas: Lyndon B. Johnson Space Center.
- Neal, C. R., Hacker, M. D., Snyder, G. A., Taylor, L. A., Liu, Y.-G., and Schmitt, R. A. 1994. Basalt Generation at the Apollo 12 Site, Part 1: New Data, Classification, and Re-Evaluation. *Meteoritics* 29: 334.
- Neal, C. R., and Taylor, L. A. 1989. The Nature of Barium Partitioning Between Immiscible Melts: A Comparison of Experimental and Natural Systems with Reference to Lunar Granite Petrogenesis. Proceedings, 19th Lunar and Planetary Science Conference. pp. 209–18.
- Neal, C. R., and Taylor, L. A. 1991. Evidence for Metasomatism of the Lunar Highlands and the Origin of Whitlockite. *Geochimica et Cosmochimica Acta* 55: 2965–80.
- Neal, C. R., and Taylor, L. A. 1992. Petrogenesis of Mare Basalts: A Record of Lunar Volcanism. *Geochimica et Cosmochimica Acta* 56: 2177–211.
- Neal, C. R., Taylor, L. A., and Lindstrom, M. M. 1988. Apollo 14 Mare Basalt Petrogenesis: Assimilation of KREEP-Like Components by a Fractionating Magma. Proceedings, 18th Lunar and Planetary Science Conference. pp. 139–53.
- Pernet-Fisher, J. F., Howarth, G. H., Liu, Y., Chen, Y., and Taylor, L. A. 2014. Estimating the Lunar Mantle Water Budget from Phosphates: Complications Associated with Silicate-Liquid-Immiscibility. *Geochimica et Cosmochimica Acta* 144: 326–41.
- Philpotts, A. R. 1971. Immiscibility Between Feldspathic and Gabbroic Magmas. *Nature Physical Science* 229: 107–9.
- Pieters, C. M., Head, J. W., Whitford-Stark, J. L., Adams, J. B., McCord, T. B., and Zisk, S. H. 1980. Late High-Titanium Basalts of the Western Maria—Geology of the Flamsteed Region of Oceanus Procellarum. *Journal of Geophysical Research* 85: 3913–38.
- Potts, N. J., Tartèse, R., Anand, M., van Westrenen, W., Griffiths, A. A., Barrett, T. J., and Franchi, I. A. 2016. Characterization of Mesostasis Regions in Lunar Basalts: Understanding Late-Stage Melt Evolution and Its Influence on Apatite Formation. *Meteoritics & Planetary Science* 51: 1555–75.
- Prettyman, T. H., Hagerty, J. J., Elphic, R. C., Feldman, W. C., Lawrence, D. J., McKinney, G. W., and Vaniman, D. T. 2006. Elemental Composition of the

- Lunar Surface: Analysis of Gamma Ray Spectroscopy Data from Lunar Prospector. *Journal of Geophysical Research: Planets* 111.
- Prissel, K. B., Krawczynski, M. J., Nie, N. X., Dauphas, N., Couvy, H., Hu, M. Y., Alp, E. E., and Roskosz, M. 2018. Experimentally Determined Effects of Olivine Crystallization and Melt Titanium Content on Iron Isotopic Fractionation in Planetary Basalts. *Geochimica et Cosmochimica Acta* 238: 580–98.
- Qian, Y. Q., Xiao, L., Zhao, S. Y., Zhao, J. N., Huang, J., Flahaut, J., Martinot, M., Head, J. W., Hiesinger, H., and Wang, G. X. 2018. Geology and Scientific Significance of the Rümker Region in Northern Oceanus Procellarum: China's Chang'E-5 Landing Region. *Journal of Geophysical Research: Planets* 123: 1407–30.
- Rhodes, J. M., Blanchard, D. P., Dungan, M. A., Brannon, J. C., and Rodgers, K. V. 1977. Chemistry of Apollo 12 Mare Basalts: Magma Types and Fractionation Processes. Proceedings, 2nd Lunar Science Conference. pp. 1305–38.
- Roedder, E. 1951. Low Temperature Liquid Immiscibility in the System K_2O - FeO - Al_2O_3 - SiO_2 . *American Mineralogist* 36: 282–6.
- Roedder, E., and Weiblen, P. W. 1970. Silicate Liquid Immiscibility in Lunar Magmas, Evidenced by Melt Inclusions in Lunar Rocks. *Science* 167: 641–44.
- Roedder, E., and Weiblen, P. W. 1977. Compositional Variation in Late-Stage Differentiates in Mare Lavas, as Indicated by Silicate Melt Inclusions. Proceedings, 2nd Lunar Science Conference. pp. 1767–83.
- Roeder, P. L., and Emslie, R. F. 1970. Olivine-Liquid Equilibrium. *Contributions to Mineralogy and Petrology* 29: 275–89.
- Rutherford, M. J., Hess, P. C., and Daniel, G. H. 1974. Experimental Liquid Line of Descent and Liquid Immiscibility for Basalt 70017. Proceedings, 11th Annual Lunar Science Conference. pp. 569–83.
- Sato, M., Hickling, N. L., and McLane, J. E. 1973. Oxygen Fugacity Values of Apollo 12, 14, and 15 Lunar Samples and Reduced State of Lunar Magmas. Proceedings, 4th Lunar and Planetary Science Conference. p. 1061.
- Sha, L.-K. 2000. Whitlockite Solubility in Silicate Melts: Some Insights into Lunar and Planetary Evolution. *Geochimica et Cosmochimica Acta* 64: 3217–36.
- Snape, J. F., Davids, B., Nemchin, A. A., Whitehouse, M. J., and Bellucci, J. J. 2018. Constraining the Timing and Sources of Volcanism at the Apollo 12 Landing Site Using New Pb isotopic Compositions and Crystallisation Ages. *Chemical Geology* 482: 101–12.
- Snape, J. F., Joy, K. H., Crawford, I. A., and Alexander, L. 2014. Basaltic Diversity at the Apollo 12 Landing Site: Inferences from Petrologic Examinations of the Soil Sample 12003. *Meteoritics & Planetary Science* 49: 842–71.
- Snape, J. F., Nemchin, A. A., Grange, M. L., Bellucci, J. J., Thiessen, F., and Whitehouse, M. J. 2016. Phosphate Ages in Apollo 14 Breccias: Resolving Multiple Impact Events with High Precision U-Pb SIMS Analyses. *Geochimica et Cosmochimica Acta* 174: 13–29.
- Stadermann, A. C., Zanetti, M. R., Jolliff, B. L., Hiesinger, H., van der Bogert, C. H., and Hamilton, C. W. 2018. The Age of Lunar Mare Basalts South of the Aristarchus Plateau and Effects of Secondary Craters Formed by the Aristarchus Event. *Icarus* 309: 45–60.
- Staid, M. I., and Pieters, C. M. 2001. Mineralogy of the Last Lunar Basalts: Results from Clementine. *Journal of Geophysical Research* 106: 27887–900.
- Takeda, H., Miyamoto, M., Duke, M. B., and Ishii, T. 1978. Crystallization of Pyroxenes in Lunar KREEP Basalt 15386 and Meteoritic Basalts. Proceedings, 11th Annual Lunar Science Conference. pp. 1157–71.
- Tartèse, R., Anand, M., Barnes, J. J., Starkey, N. A., Franchi, I. A., and Sano, Y. 2013. The Abundance, Distribution, and Isotopic Composition of Hydrogen in the Moon as Revealed by Basaltic Lunar Samples: Implications for the Volatile Inventory of the Moon. *Geochimica et Cosmochimica Acta* 122: 58–74.
- Tartèse, R., Anand, M., and Delhaye, T. 2013. NanoSIMS Pb/Pb Dating of Tranquillityite in High-Ti Lunar Basalts: Implications for the Chronology of High-Ti Volcanism on the Moon. *American Mineralogist* 98: 1477–86.
- Tartèse, R., Anand, M., McCubbin, F. M., Elardo, S. M., Shearer, C. K., and Franchi, I. A. 2014. Apatites in Lunar KREEP Basalts: The Missing Link to Understanding the H isotope Systematics of the Moon. *Geology* 42: 363–6.
- Taylor, G. J., Warren, P., Ryder, G., Delano, J., Pieters, C., and Lofgren, G. 1991. Lunar Rocks. In *Lunar Sourcebook: A User's Guide to the Moon*, edited by G. H. Heiken, D. T. Vaniman, and B. M. French, 183–284. Cambridge, UK: Cambridge University Press. 736 p.
- Tian, H.-C., Wang, H., Chen, Y., Yang, W., Zhou, Q., Zhang, C., Lin, H.-L. et al. 2021. Non-KREEP Origin for Chang'E-5 Basalts in the Procellarum KREEP Terrane. *Nature* 600: 59–63.
- Toplis, M. J., Libourel, G., and Carroll, M. R. 1994. The Role of Phosphorous in Crystallization Processes of Basalt: An Experimental Study. *Geochimica et Cosmochimica Acta* 58: 797–810.
- Veksler, I. V., Dorfman, A. M., Borisov, A. A., Wirth, R., and Dingwell, D. B. 2007. Liquid Immiscibility and the Evolution of Basaltic Magma. *Journal of Petrology* 48: 2187–210.
- Wadhwa, M. 2008. Redox Conditions on Small Bodies, the Moon and Mars. *Reviews in Mineralogy and Geochemistry* 68: 493–510.
- Wänke, H., Wlotzka, F., Baddenhausen, H., Balacescu, A., Spettel, B., Teschke, F., Jagoutz, E., Kruse, H., Quijano-Rico, M., and Rieder, R. 1971. Apollo 12 Samples: Chemical Composition and Its Relation to Sample Locations and Exposure Ages, the Two-Component Origin of the Various Soil Samples and Studies on Lunar Metallic Particles. Proceedings, 2nd Lunar Science Conference. p. 1187.
- Warren, P. H., and Wasson, J. T. 1979. The Origin of KREEP. *Reviews of Geophysics and Space Physics* 17: 73–88.
- Wentworth, S. J. J., McKay, D. S., Lindstrom, D. J., Basu, A., Martinez, R. R., Bogard, D. D., and Garrison, D. H. 1994. Apollo 12 Ropy Glasses Revisited. *Meteoritics* 29: 323.
- Wieczorek, M. A., Jolliff, B. L., Khan, A., Pritchard, M. E., Weiss, B. P., Williams, J. G., Hood, L. L. 2006. The Constitution and Structure of the Lunar Interior. In *New Views of the Moon*, edited by B. L. Jolliff, M. A. Wieczorek, C. K. Shearer, and C. R. Neal. Reviews in Mineralogy and Geochemistry 60: 221–364.
- Yoder, H. S. 1979. *Evolution of the Igneous Rocks: Fiftieth Anniversary Perspectives*. Princeton, New Jersey: Princeton University Press.

SUPPORTING INFORMATION

Additional supporting information may be found in the online version of this article.

Table S1. Reagents used in petrologic experiments.

Table S2. Gas mixtures for experiments.

Table S3. Sample 12032,366-18 data—Olivine.

Table S4. Sample 12032,366-18 data—Augite.

Table S5. Sample 12032,366-18 data—Pigeonite.

Table S6. Sample 12032,366-18 data—Ferropyrroxene.

Table S7. Sample 12032,366-18 data—Plagioclase.

Table S8. Sample 12032,366-18 data—Ilmenite.

Table S9. Sample 12032,366-18 data—Barian K-feldspar.

Table S10. Sample 12032,366-18 data—K-feldspar.

Table S11. Sample 12032,366-18 data—Ti-chromite.

Table S12. Sample 12032,366-18 data—Cr-ulvöspinel.

Table S13. Sample 12032,366-18 data—Merrillite.

Table S14. Sample 12032,366-18 data—Apatite.

Table S15. Sample 12032,366-18 data—Zircon.

Table S16. Sample 12032,366-18 data—Silica.

Table S17. Sample 12032,366-18 data—Troilite.

Table S18. Sample 12032,366-18 data—Felsic mesostasis.

Table S19. Sample 12032,366-18 data—Mafic mesostasis.

Table S20. Experimental data—Overview.

Table S21. Experimental data—H028.

Table S22. Experimental data—J024.

Table S23. Experimental data—J157.

Table S24. Experimental data—H168.

Table S25. Experimental data—J146.